Journal of Computational Physics 566 (2026) 115277

Contents lists available at ScienceDirect

Journal of Computational Physics

journal homepage: www.elsevier.com/locate/jcp

# Asymptotic global spectral analysis of physical and spurious modes in three-level time-integration methods applied to Fourier-discretised convection-diffusion dynamics

A. Boguslawski [a,*], A. Tyliszczak [a], B. J. Geurts [b,c,d]

[a] Czestochowa University of Technology, Faculty of Mechanical Engineering, Al. Armii Krajowej 21, Czestochowa, 42-201, Poland
[b] Mathematics of Multiscale Modeling and Simulation, Faculty EEMCS, University of Twente, P.O. Box 217, Enschede, 7500AE, the Netherlands
[c] Multiscale Physics, Faculty of Technical Physics, Eindhoven University of Technology, P.O. Box 513, Eindhoven, 5600MB, the Netherlands
[d] Computational Science, Centrum voor Wiskunde en Informatica, Science Park 123, Amsterdam, 1098XG, the Netherlands

ARTICLE INFO

*Keywords:*
Time-integration
Global spectral analysis
Spectral discretisation
Adams-Bashforth
Adams-Moulton
Convection-diffusion
Spurious modes

ABSTRACT

Global Spectral Analysis (GSA) is applied to the three-time-level second-order Adams–Bashforth (AB) and third-order Adams–Moulton (AM) time-integration methods to analyze the physical and spurious modes that occur in a spectrally discretized convection–diffusion equation. We develop an iterative procedure that enables GSA to be applied both (i) immediately after an initialization performed with a two-time-level method and (ii) at all subsequent time steps, until an asymptotically converged state (ACS) is reached. It is shown that, in ACS, the domains of influence of the physical and spurious modes on the stability plane (i.e., the distribution of amplification factors in Courant–Friedrichs–Lewy (CFL) / wave number coordinates) and their magnitudes differ significantly from those obtained immediately after initialization. In this regard, we show that: (a) Determining the stability limit solely from the stability map generated immediately after initialization leads to an incorrect estimate of the allowable CFL number. Long-term simulations performed with a CFL number close to the incorrectly predicted "critical" value eventually may become unstable. The correct critical CFL number can only be assessed once ACS is reached. (b) The influence of the two-time-level initialization method on the physical and spurious modes is only temporary and completely vanishes in ACS. Thus, the particular choice of initialization has a negligible impact on the solution for sufficiently long simulation times. (c) The simultaneous influence of physical and spurious modes on specific solution length scales is also transient. In ACS, each length scale evolves under the dynamics of either the physical mode or the spurious mode, but not both. We demonstrate that the stability plane is divided into regions where the presence of one mode precludes the occurrence of the other.

To investigate the influence of viscous effects on these characteristics, we introduce the Péclet number ($Pe$), which combines the viscosity coefficient, time step, and mesh spacing. Within the stability limits (i.e., for Péclet and CFL numbers below their critical values), three regions are identified. (1) Physical-mode dominated region where the spurious mode has no influence on the solution. The physical mode governs the dynamics at all length scales. This corresponds to small Péclet numbers, $Pe < 2/(9\pi^2)$ for the Adams-Bashforth method and $Pe < 6/(7\pi^2)$ for the Adams-Moulton method. (2) Conditional spurious-mode region (for AB: $2/(9\pi^2) < Pe < 2/(3\pi^2)$, for AM:

* Corresponding author.
*E-mail address:* andrzej.boguslawski@pcz.pl (A. Boguslawski).

https://doi.org/10.1016/j.jcp.2026.115277
Received 4 February 2026; Received in revised form 24 July 2026; Accepted 3 August 2026
Available online 6 August 2026

$6/(7\pi^2) < Pe < 3/(2\pi^2)$) where the influence of the spurious mode can be avoided by selecting a sufficiently small CFL number. Otherwise, small-scale features are governed by the spurious mode, while large-scale features remain governed by the physical mode. (3) Spurious-mode dominated region (AB: $Pe > 2/(3\pi^2)$, AM: $Pe > 3/(2\pi^2)$) where the impact of the spurious mode cannot be avoided. It exclusively governs the evolution of small solution scales.

## 1. Introduction

Global spectral analysis (GSA) is a crucial tool for characterizing the spatiotemporal properties of numerical solutions, including stability, numerical phase speed, numerical diffusion, and group velocity. GSA has been presented in detail in a recent paper by Sagaut et al. [1] which discusses a series of contributions by T.K. Sengupta and co-workers [2–5], in which GSA has been extensively used to determine the solution and error dynamics of the 1D linear convection equation discretized using various spatial schemes (finite differences, compact differences, Fourier spectral method) and integrated in time by applying two-time-level Runge–Kutta methods up to fourth order. GSA has enabled the determination of stability maps and distributions of numerical phase speed, numerical diffusion, and group velocity as functions of the Courant–Friedrichs–Lewy (CFL) number, wave number, and the Péclet number. Theoretical findings and recommendations were validated using several test cases, including problems with analytical solutions, such as traveling Gaussian pulses or wave packets, and acoustic wave propagation. Also, more complex fluid-flow problems governed by the Navier–Stokes equations can be addressed in GSA. Recently, GSA was developed by Suman et al. [6], for the two-dimensional convection-diffusion equation discretised with the pseudo-spectral method combined with the second and fourth order Runge-Kutta schemes, showing poor stability of the second-order method. The accuracy of GSA was highlighted through long-term simulations of the 2D Taylor-Green vortex in the vorticity-stream function formulation of the Navier-Stokes equations.

The stability and accuracy of time-integration methods for solving the Navier–Stokes equations have also been the subject of separate comparative studies [7,8], with attention paid to their suitability for Direct Numerical Simulation (DNS) [9,10]. The theoretical analysis in these works was limited to the 1D convection equation, specifically addressing Runge–Kutta methods and a three-level Adams–Bashforth method. In general, efficient multi-level methods are essential for achieving higher-order temporal accuracy while minimizing the number of spatial-discretization evaluations. However, multi-level methods can admit spurious solution modes that can contaminate the physically relevant dynamics [11]. In the case of the second-order Adams–Bashforth method, the physical and spurious modes were first discussed by Lilly [12], who concluded that the influence of the spurious mode on the solution was negligible. Much later, Durran [13] expressed the same view. However, in light of more recent studies [4,7,8], this conclusion appears to be incomplete, motivating also the current study. It has been shown that the magnitudes of the physical and spurious modes depend strongly on the spatial discretization scheme and the adopted bootstrapping method [1,4]. Such bootstrapping refers to the procedure used to generate the solution at the first time step ($n = 1$) from the initial condition ($n = 0$). This step is necessary for three-level methods, which advance the solution in time starting from $n = 2$, using the values at $n = 1$ and $n = 0$. Surprisingly, throughout the literature, the analyses of the physical and spurious modes end at time step $n = 2$ in terms of stability maps. The stability maps indicate the maximum allowable CFL numbers for stable integration and provide an overview that allows the solution dynamics to be anticipated based on the distributions of the numerical phase speed, numerical viscosity, and group velocity. It has been put forward that the physical and spurious modes coexist for $n > 3$, and that their combined influence on the solution depends largely on the wavelengths at which they act. For instance, in [7,8], it has been suggested, based on the pure convection equation, that the Adams–Bashforth method should not be used for DNS, since the presence of the spurious mode leads to damping of high-frequency solution components (small-scale flow phenomena), removing energy from the system. On the other hand, it is well known that this method has been successfully applied in DNS studies and has produced accurate and widely cited results, e.g., [14,15]. This remarkable situation motivates the current analysis, which includes asymptotic stability maps to fully assess the occurrence and influence of spurious modes on the overall solution. In fact, the analysis of these three - or higher time level methods for the more complete convective-diffusive systems has been pioneered in [1], indicating that the observed performance of the method is linked to the actual dissipation of the spurious mode itself in the diffusive system, which may strengthen stability without affecting accuracy. Here, we focus explicitly on asymptotic stability for three-level methods.

GSA of solution methods for the convection–diffusion equation has been performed in [16], focusing on the fourth-order Runge–Kutta method for time integration combined with central and upwind schemes for spatial discretization, and in [17], where the Adams–Bashforth and Crank–Nicolson methods were used for the convective and diffusive term time integration respectively. In [17], two spatial discretization approaches were considered, namely Fourier spectral and second-order central-difference schemes. As in the pure convection problem, physical and spurious modes were observed for the convection–diffusion equation when the Adams–Bashforth method was employed. In this case, it was demonstrated that, in addition to their dependence on the spatial discretization scheme, the presence of physical and spurious modes also depends on the strength of the viscous forces, although this aspect was only briefly explored. As in previous studies, the analysis was limited to the time step $n = 2$, and conclusions drawn from the stability map were extrapolated to all subsequent time steps.

The present work deliberately focuses on the linear convection–diffusion equation because it provides the simplest model that still captures the two fundamental transport mechanisms governing the Navier–Stokes equations, namely convection and diffusion. Despite its seemingly simple nature, this model problem exhibits the dynamic richness expected from the application of Adams-Bashforth and Adams-Moulton time integration. This choice enables a systematic investigation of the dispersive, dissipative, and stability properties of multi-level time-integration methods without the additional complexities introduced by nonlinear terms. In

particular, the characteristic equation of the three-level schemes studied here reduces to a quadratic polynomial, allowing the complete stability and mode analysis to be carried out analytically using only algebraic manipulations. This analytical framework enables the isolation and quantification of the roles of physical and spurious modes, providing explicit insights into the conditions that give rise to spurious modes. The study, therefore, represents a deliberate first step toward the analysis of more realistic problems, building on the foundational work of T.K. Sengupta [4] and forming the basis for ongoing research on increasingly more complex flow equations.

The convection and diffusion terms are discretized in space using the Fourier spectral method. The analysis focuses on establishing stability restrictions for time integration, illustrated by various numerical solution properties (e.g., phase speed, viscosity, group velocity) in the Péclet-Courant–Friedrichs–Lewy ($Pe$-CFL) domain. Unlike in [17], we do not terminate GSA at time step $n = 2$. Instead, we formulate an iterative framework that enables a complete analysis also in cases where the solution converges asymptotically to a stable state (ACS - asymptotically converged state). We show that the coexistence of physical and spurious modes reported in the literature [1,7,17] is only temporary and occurs solely during the transient stage following the two-time-level initialization procedure. Consequently, and in contrast to what has been established for the Adams–Bashforth method (and other multi-level integrators, e.g., the leapfrog method [4]), we demonstrate that at ACS, the solution length scales are governed either by the physical or the spurious mode dynamics, but not simultaneously by both, whereas the stability condition corresponds exactly to the one formulated by Dahlquist [18]. We further demonstrate that this behavior also applies to the Adams–Moulton method, which, like the Adams–Bashforth scheme, is a three-level, third-order implicit method. For both methods, we identify regions in the $Pe$–CFL domain that are completely free of spurious mode contributions, next to regions where physical/spurious modes affect some range of scales, and regions where spurious modes fully dominate the temporal advancement. The regions free from spurious modes are shown to have low Péclet numbers, i.e., fine spatial resolution, complementing the advice against the use of the Adams-Bashforth method in [7,8].

While the conceptual foundation of our analysis aligns with classical stability theory, such as Dahlquist's theorem [18], our study provides a vital bridge between this theory and practical numerical implementations of the Adams-Bashforth and the Adams-Moulton [19] integration methods. The main result of this paper are the comprehensive stability diagrams, parametrized by Péclet and CFL numbers. These diagrams yield quantitative bounds that explicitly define the onset of spurious modes and instabilities. To our knowledge, the analytical determination of these critical Péclet thresholds has not been previously demonstrated. By explicitly charting the different asymptotic stability regimes, our work translates intuitively expected behavior into practical insights, providing users of these well-studied methods with rigorous and readily applicable diagnostic tools.

The organization of this paper is as follows. The global spectral analysis of the convection-diffusion equation is introduced in Section 2. Subsequently, characteristics of the discrete solutions across all resolved modes are presented for the Adams-Bashforth and Adams-Moulton methods, as functions of the CFL number and the wave-number, at a range of Péclet numbers in Section 3. This provides a detailed assessment of parameters and scale regions in which (un)stable dynamics emerges, with and without spurious modes. A summarizing overview of the dynamical stability as a function of Péclet and CFL numbers is presented and discussed in Section 4. Solution accuracy at specific points in the stability diagrams is discussed in Section 5. Concluding remarks are presented in Section 6.

## 2. Global spectral analysis of multi-step methods

In this Section, we first present the framework for global spectral analysis and introduce several characteristic quantities used to quantify the findings. Subsequently, we define physical and spurious modes and analyze their role in the computational dynamics of convection-diffusion problems.

### 2.1. Global spectral analysis framework for convection-diffusion problems

We consider the linear convection-diffusion equation

$$\frac{\partial u}{\partial t} + c\frac{\partial u}{\partial x} = \nu\frac{\partial^2 u}{\partial u^2} \tag{1}$$

where $x, t$ denote the spatial and temporal variables, and the positive constants $c$ and $\nu$ denote the convection speed and the coefficient of diffusion, respectively. Within a global spectral analysis [4], the solution $u(x,t)$ is studied in conjunction with its Fourier transform, that is,

$$u(x,t) = \int \hat{U}(k,t)e^{ikx}dk \tag{2}$$

where $\hat{U}$ is the Fourier transform, $i$ is the imaginary unit, and $k$ stands for the wave number. Substituting (2) in the convection-diffusion equation leads to the equivalent formulation in the spectral space

$$\frac{d\hat{U}}{dt} + ick\hat{U} = -\nu k^2\hat{U} \tag{3}$$

The convection-diffusion equation is solved for an initial condition

$$u(x,0) = u_0(x) = \int \hat{U}_0(k)e^{ikx}dk \tag{4}$$

In spectral space, the exact solution reads

$$\widehat{U}(k,t) = \widehat{U}_0(k) e^{-\nu k^2 t} e^{-ikct} \tag{5}$$

Introducing the bi-dimensional Fourier transform

$$u(x,t) = \int\int \widehat{U}(k,\omega) e^{i(kx-\omega t)}\, dk\, d\omega \tag{6}$$

into the convection-diffusion Eq. (1) yields

$$\int\int \widehat{U}(k,\omega)\Big[\frac{\partial}{\partial t} e^{i(kx-\omega t)} + c\frac{\partial}{\partial x} e^{i(kx-\omega t)}\Big]\, dk\, d\omega = \nu \int\int \widehat{U}(k,\omega)\frac{\partial^2}{\partial x^2} e^{i(kx-\omega t)}\, dk\, d\omega \tag{7}$$

and allows for finding the following dispersion relation:

$$-i\omega + ick = -\nu k^2 \implies \omega = ck - i\nu k^2 \tag{8}$$

Here, $\omega$ stands for the circular frequency. The real part represents the oscillatory frequency, and the imaginary part represents the amplitude damping. As stressed by Suman et al. [16], the dispersion relation is an important property for wave propagation problems. It describes the phase speed and group velocities of the signals. A numerical scheme used to solve such problems should ideally reproduce these aspects as closely as possible to accurately predict wave propagation. From the above dispersion relation, one can obtain the complex physical phase speed as

$$c_{phys} = \frac{\omega}{k} = c - i\nu k \tag{9}$$

and the real part of the physical group velocity

$$V_{g,phys} = \mathrm{Re}\Big(\frac{\partial \omega}{\partial k}\Big) = \mathrm{Re}(c - 2i\nu k) = c \tag{10}$$

These different velocities characterize key aspects of the advection-diffusion dynamics, which will be used momentarily to analyze properties of numerical integration. For convenience, the accuracy and stability of the solution will be analyzed in terms of dimensionless quantities, the CFL ($N_c$) and the Péclet ($Pe$) numbers, which combine the physical ($c$, $\nu$) and numerical solution parameters. They are defined as $N_c = c\Delta t/h$ and $Pe = \nu\Delta t/h^2$, where $h$ is the mesh spacing and $\Delta t$ is the time-step.

The physical growth rate of the solution in time can easily be obtained from (5), and we are particularly interested in changes in the solution on the scale of $\Delta t$. Knowing $\widehat{U}(k,t)$ at two consecutive time-steps, their ratio defines the amplification in the form

$$\begin{aligned} G_{phys} = \frac{\widehat{U}(k,t+\Delta t)}{\widehat{U}(k,t)} &= e^{-\nu k^2 \Delta t} e^{-ikc\Delta t} \equiv e^{-i\omega\Delta t} \\ &= e^{-Pe(kh)^2} e^{-iN_c(kh)} = |G_{phys}| e^{-i\beta} \end{aligned} \tag{11}$$

where $|G_{phys}| = e^{-\nu k^2 \Delta t} = e^{-Pe(kh)^2}$ is the amplificaton factor module and $\beta = kc\Delta t$ is the phase angle. The numerical dispersion relation is formulated similarly to the exact dispersion relation for the convection-diffusion equation, as

$$\omega_{num} = kc_{num} - i\nu_{num} k^2 \tag{12}$$

in terms of the numerical phase speed $c_{num}$ and the numerical coefficient of diffusion $\nu_{num}$ (not to be confused with the numerical viscosity introduced by upwind-type schemes). Using the numerical dispersion relation, the numerical amplification factor is obtained as

$$G_{num} = e^{-i\omega_{num}\Delta t} = e^{-\nu_{num} k^2 \Delta t} e^{-ikc_{num}\Delta t} \equiv |G_{num}| e^{-i\beta_{num}}, \tag{13}$$

where $|G_{num}| = e^{-\nu_{num} k^2 \Delta t}$ is the modulus of the numerical amplification factor and $\beta_{num} = kc_{num}\Delta t$ is the numerical phase angle. Noting that $|G_{num}| > 1 \rightarrow \nu_{num} < 0$ implies the stability condition to be $|G_{num}| \leq 1$. Simultaneously, expressing $|G_{num}|$ as

$$|G_{num}| = e^{-\nu_{num}/\nu\, Pe(kh)^2} = |G_{phys}|^{\nu_{num}/\nu} \tag{14}$$

it is clear that for stable conditions in which $|G_{phys}| < 1$ we have: if $\nu_{num} < \nu \rightarrow |G_{num}| > |G_{phys}|$ and if $\nu_{num} > \nu \rightarrow |G_{num}| < |G_{phys}|$. Correspondingly, the numerical solution may exhibit a weaker or stronger damping than the physical solution, depending on how $\nu_{num}$ relates to $\nu$. In the following sections, we will demonstrate that for specific combinations of $N_c$ and $Pe$, the solution can be significantly deteriorated, i.e., the numerical solution deviates substantially from the exact physical solution, especially at high wave numbers.

### 2.2. Numerical phase speed, group velocity and diffusivity

To analyze the relations between the numerical and physical phase speed, group velocity, and diffusion coefficient, they are, for convenience, expressed in terms of $(kh)$, $Pe$, and $N_c$. Having computed $G_{num}$ and using (13), the numerical phase angle over a time $\Delta t$ can be calculated from

$$\tan\left(\beta_{num}\right) = -\frac{\mathrm{Im}(G_{num})}{\mathrm{Re}(G_{num})} \tag{15}$$

Simultaneously, noting that $c_{num} = \beta_{num}/k\Delta t$, the ratio of numerical to physical phase speed is given as

$$\frac{c_{num}}{c} = \frac{\beta_{num}}{kc\Delta t} = -\frac{1}{N_c(kh)} \tan^{-1}\left(\frac{\mathrm{Im}(G_{num})}{\mathrm{Re}(G_{num})}\right) \tag{16}$$

The ratio of the numerical to physical diffusion coefficients is obtained from (14) and reads as

$$\frac{\nu_{num}}{\nu} = -\frac{\ln(|G_{num}|)}{Pe(kh)^2} \tag{17}$$

Taking into account only the real part of the numerical dispersion relation (12), the numerical group velocity is defined as

$$\begin{aligned} V_{g,num} = \mathrm{Re}\left(\frac{\partial \omega_{num}}{\partial k}\right) &= c_{num} + k\frac{dc_{num}}{dk} \\ &= c_{num} + k\frac{d}{dk}\left(\frac{\beta_{num}}{k\Delta t}\right) \\ &= c_{num} + \frac{1}{\Delta t}\frac{d\beta_{num}}{dk} - \frac{1}{k\Delta t}\beta_{num} \\ &= \frac{1}{\Delta t}\frac{d\beta_{num}}{dk} \end{aligned} \tag{18}$$

Hence, the ratio of the numerical to the physical group velocity can be defined as

$$\frac{V_{g,num}}{V_{g,phys}} = \frac{V_{g,num}}{c} = \frac{1}{N_c}\frac{d\beta_{num}}{d(kh)} \tag{19}$$

### 2.3. Physical and spurious modes

GSA will be applied to Fourier spectral differentiation [19,20] of both terms of the convection-diffusion Eq. (1). The Fourier method is indispensable for advanced studies of fluid flow problems and is essential for achieving high-fidelity DNS and Large Eddy Simulations [10,21]. Note that applying Fourier differentiation allows us to focus solely on the properties of the time integration methods. Otherwise, for example, when using a finite-difference method, the analysis would also depend on the order of discretization. As will be shown momentarily, this can also be easily taken into account even if (1) is transformed into spectral space.

Introducing a spatial operator of (1) in a form

$$L = -c\frac{\delta}{\delta x} + \nu\frac{\delta^2}{\delta x^2}, \tag{20}$$

where $\delta/\delta x$, $\delta^2/\delta x^2$ denote discrete Fourier approximations of the first and second order derivatives, the Adams–Bashforth and Adams–Moulton methods, hereafter denoted as AB and AM, read as

$$AB: \quad \frac{U^{n+1} - U^n}{\Delta t} = \frac{3}{2}LU^n - \frac{1}{2}LU^{n-1} \tag{21}$$

$$AM: \quad \frac{U^{n+1} - U^n}{\Delta t} = \frac{5}{12}LU^{n+1} + \frac{8}{12}LU^n - \frac{1}{12}LU^{n-1} \tag{22}$$

where the superscripts $n-1$, $n$, and $n+1$ denote the previous, current, and next time level, respectively.

To simplify the notation and perform the analysis in the non-dimensional framework, we introduce the following notation for the spectral form of the convection-diffusion Eq. (3)

$$\begin{aligned} \frac{d\hat{U}}{dt} &= -ick\hat{U} - \nu k^2\hat{U} \\ &= \frac{-iN_c(kh) - Pe(kh)^2}{\Delta t}\hat{U} \equiv \frac{L^{Fo}}{\Delta t}\hat{U} \end{aligned} \tag{23}$$

where $L^{Fo}$ represents (20) in spectral space, expressed in terms of $N_c$ and $Pe$.

The above-formulated equations can be readily generalized to a finite/compact difference scheme of arbitrary order and type, e.g., central or upwind. This can be done by incorporating the modified wave number [22,23] in the term stemming from the Fourier differentiation of the first/second order derivative ($kh$, $(kh)^2$). For example, taking $kh \to \sin(kh)$, $(kh)^2 \to 2 - 2\cos(kh)$ would be equivalent to applying the second-order finite difference scheme. Formulas for modified wave numbers associated with the finite/compact difference schemes can be found in various sources. In [24], they are given up to the 24th order of approximation. Applying such methodology would enable GSA for various discretization methods and their combinations. This, however, is left for future studies, and in the sequel, we focus entirely on the Fourier spectral method.

The AB method applied to (3) reads as

$$\hat{U}^{n+1} = \left(1 + \frac{3}{2}L^{Fo}\right)\hat{U}^n - \frac{1}{2}L^{Fo}\hat{U}^{n-1} \tag{24}$$

and the AM method is formulated as

$$\left(1-\frac{5}{12}L^{Fo}\right)\hat{U}^{n+1}=\left(1+\frac{8}{12}L^{Fo}\right)\hat{U}^{n}-\frac{L^{Fo}}{12}\hat{U}^{n-1} \tag{25}$$

Defining an asymptotic, i.e., $n$-independent, amplification factor $G^{AB}$ for the AB method as

$$G^{AB}=\frac{\hat{U}^{n+1}}{\hat{U}^{n}}=\frac{\hat{U}^{n}}{\hat{U}^{n-1}} \tag{26}$$

we may derive an algebraic equation for $G^{AB}$ from (24) upon dividing by $\hat{U}^n$ as

$$G^{AB}=\left(1+\frac{3}{2}L^{Fo}\right)-\frac{1}{2}\frac{L^{Fo}}{G^{AB}} \tag{27}$$

which can be rearranged into the following quadratic equation for $G^{AB}$:

$$\left(G^{AB}\right)^2-\left(1+\frac{3}{2}L^{Fo}\right)G^{AB}+\frac{1}{2}L^{Fo}=0 \tag{28}$$

with two solutions

$$G^{AB}_{\pm}=\frac{1}{2}\left(1+\frac{3}{2}L^{Fo}\pm\sqrt{\Delta}\right) \tag{29}$$

where the discriminant $\Delta$ is defined as

$$\Delta=\left(1+\frac{3}{2}L^{Fo}\right)^2-2L^{Fo}=1+(kh)^2\left[\frac{9}{4}\left(N_c^2+Pe^2(kh)^2\right)-Pe\right]+iN_c(kh)\left[\frac{9}{2}Pe(kh)^2-1\right] \tag{30}$$

Following the argumentation of Sengupta [4] and Sagaut et al. [1], the physical mode is the one of the two solutions for which the amplification factor approaches the physical amplification factor when the time step tends to zero. In contrast, the spurious mode has an amplification factor that tends to zero as $\Delta t\to 0$. From (23) it becomes clear that $L^{Fo}\to 0$ when $\Delta t\to 0$. Simultaneously, $G^{AB}_{+}\to 1$ (as $G_{phys}\to 1$ in (11)), while $G^{AB}_{-}\to 0$. Hence, $G^{AB}_{+}=:G^{AB}_{phys}$ is interpreted as the amplification factor of the physical mode, and $G^{AB}_{-}=:G^{AB}_{spur}$ is the amplification factor of the spurious mode. For $h$, $\Delta t>0$, and the combination of $Pe$ and $N_c$ such that the discriminant $\Delta\neq 0$, both $G^{AB}_{phys}$ and $G^{AB}_{spur}$ simultaneously exist. Fig. 1 shows their level-sets in a $kh-N_c$ plane for $Pe=0.01$, $Pe=0.05$, and $Pe=0.20$. These $Pe$-values are selected as representative of significantly different stability maps. Note that $kh\in[0,\pi]$, with the upper limit determined by the grid cut-off wavenumber, according to the Nyquist sampling theorem. For $N_c$, there is no theoretical upper bound, however, following [7,16], it is limited here to the range $N_c\in[0,\pi]$.

As can be seen, $G^{AB}_{phys}$ and $G^{AB}_{spur}$ coexist with an increasing importance of the latter for larger $Pe$. Correspondingly, spurious modes can become more and more detrimental for the solution at sufficiently high $Pe$. For $Pe=0.05$ and $Pe=0.20$, regions with $|G^{AB}_{spur}|>1$ are present. Thus, solution modes evolving in time corresponding to $|G^{AB}_{spur}|>1$ are unstable. Special locations are points P ($kh_0=\sqrt{2/(9Pe)}$ - green line, $N_{c,0}=4/3\sqrt{Pe}$) where $|G^{AB}_{phys}|=|G^{AB}_{spur}|$. On their left sides, i.e., for $N_c<N_{c,0}$, the values of $|G^{AB}_{phys}|$ and $|G^{AB}_{spur}|$ vary smoothly and $|G^{AB}_{phys}|>|G^{AB}_{spur}|$. On the right sides of the points P ($N_c>N_{c,0}$), the situation is significantly different. An arbitrarily small deviation $\epsilon$ from $kh_0$ causes that $|G^{AB}_{phys}|$ and $|G^{AB}_{spur}|$ to abruptly change from small/large values. For instance, for $Pe=0.05$ and $N_c=0.4$ with $\epsilon=10^{-15}$ one obtains

$$\begin{aligned}&|G^{AB}_{phys}|=1.1055,\ |G^{AB}_{spur}|=0.3944 \quad \text{at} \quad kh=kh_0-\epsilon\\ &|G^{AB}_{phys}|=0.3944,\ |G^{AB}_{spur}|=1.1055 \quad \text{at} \quad kh=kh_0\end{aligned} \tag{31}$$

The reason for such an abrupt change in $|G^{AB}_{phys,spur}|$ and their 'symmetry' around $kh=kh_0-\epsilon/2$ is the change of sign of $\mathrm{Im}(\Delta)$ and in consequence the sign of $\mathrm{Im}(\sqrt{\Delta})$. These properties will be discussed later in Section 4 to characterize the stability regions in $Pe-N_c$ coordinates.

From the results presented in Fig. 1, it is seen that the spurious mode defines the stability border ($G=1$) starting from $N_c=0.3727$ for $Pe=0.05$ and $N_c=0.7454$ for $Pe=0.2$. It also determines the critical $N_c$ for which the solution remains stable, which is understood as $\min(N_c)$ on the $|G^{AB}|=1$ isoline. For $Pe=0.05$ it occurs at $kh=\pi$ and equals $N_{c,stab}=0.2475$, whereas for $Pe=0.2$ there is no $N_c$ for which both $|G^{AB}_{phys}|<1$ and $|G^{AB}_{spur}|<1$ over the entire $kh$ range. Hence, solution components evolving in time with $|G^{AB}_{phys}|>1$ or $|G^{AB}_{spur}|>1$ will be unstable. Such a situation can also be expected in the region where $|G^{AB}_{phys}|<1$ and $|G^{AB}_{spur}|<1$ if both contribute to advancing the solution in time. To analyze this issue, following [7], we define the total amplification factor $G^{AB}_{tot}$ as

$$G^{AB}_{tot}=\alpha_{phys}G^{AB}_{phys}+\alpha_{spur}G^{AB}_{spur} \tag{32}$$

where $\alpha_{phys}$ and $\alpha_{spur}$ denote factors weighing the contributions of physical and spurious modes, constrained such that

$$\alpha_{phys}+\alpha_{spur}=1. \tag{33}$$

An analysis of $G^{AB}_{tot}$ for the convection equation ($Pe=0$), discretized using finite-difference and compact-difference methods, was presented in [1,4,7,8], and for the spectral method in [17]. These studies also examined the physical and spurious components of the phase and group velocity, as well as the numerical viscosity. It has been demonstrated that the spurious mode produces nonphysical results due to the sign of the group velocity (opposite to that of the physical mode) and its strong damping effect. High-frequency

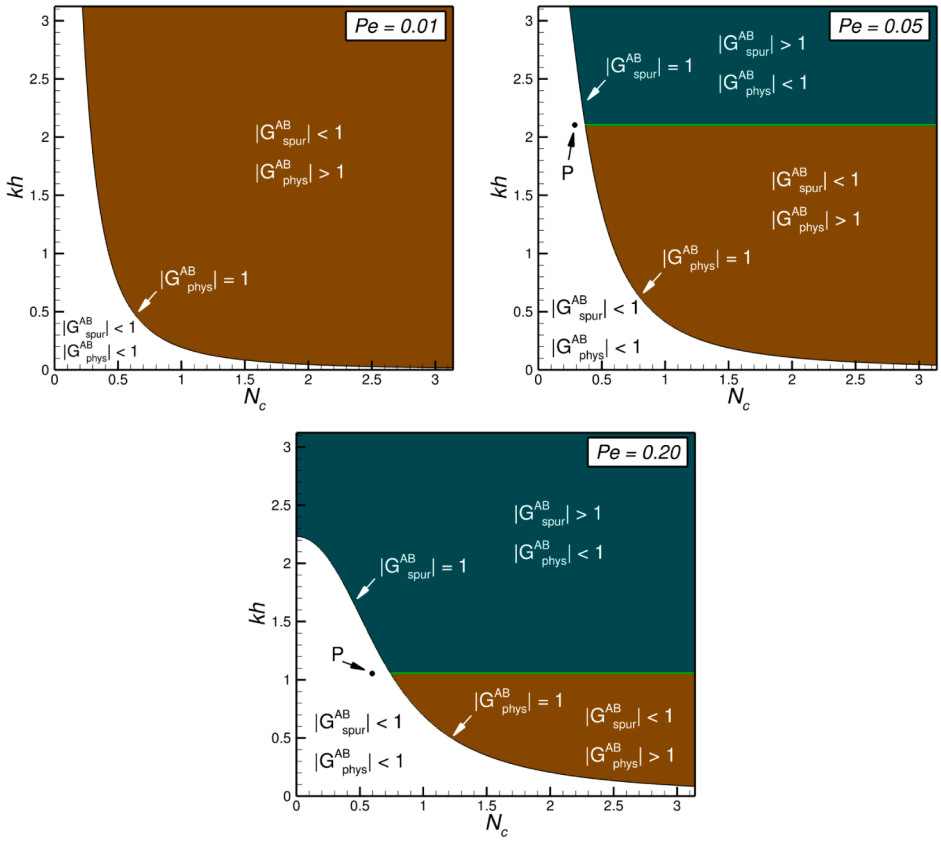


**Fig. 1.** Amplification factors corresponding to the physical ($G^{AB}_{phys}$) and spurious ($G^{AB}_{spur}$) modes for Péclet numbers $Pe = 0.01, 0.05, 0.2$. The point P indicates the location where $|G^{AB}_{phys}| = |G^{AB}_{spur}|$. Black line - the stability border where $|G^{AB}_{phys}| = 1$ or $|G^{AB}_{spur}| = 1$, green line - the discontinuity line at $kh = \sqrt{2/(9Pe)}$. (For interpretation of the references to colour in this figure legend, the reader is referred to the web version of this article.)

components of the initial solution that fall within the spurious-mode stability region are severely attenuated. For this reason, it has been concluded that the AB method should not be used in DNS, where precise representation of small-scale high-frequency phenomena is crucial. For the convection–diffusion equation, the presence of both physical and spurious modes in the solution obtained using the combination of AB and Crank–Nicolson methods has been briefly discussed in [17]. Based on several selected Péclet numbers, it has been shown that the spurious mode can become dominant in determining the stability limit.

The analyses of the physical and spurious modes presented in the above-discussed papers, however, were limited to the second time step only ($n = 2$), which follows the $n = 1$ step, where the solution is obtained using a two-time-level method starting from the initial solution at $n = 0$. We note that such an initialization procedure, sometimes referred to as bootstrapping, is necessary for multi-level methods, as an $M$-level method requires knowledge of the solutions at the previous $M - 1$ time levels. We examine how the contributions of $G_{phys}$ and $G_{spur}$ to $G_{tot}$ evolve for time steps $n > 2$, first for the AB method and then for the AM method. We show that although $G_{tot}$ initially depends on both $G_{phys}$ and $G_{spur}$, it gradually becomes dominated exclusively by either $G_{phys}$ or $G_{spur}$. Furthermore, we demonstrate that the domains of their influence shift relative to those identified for $n = 2$. Consequently, $N_{c,crit}$ differs from the value obtained for $n = 2$, implying that using the initial value leads to instability in long-term simulations. Additionally, contrary to what has been reported on the use of the AB method for the convection equation in [7,8] and subsequent works, we show that small-scale phenomena (large $kh$) within the part of the stability map governed by the spurious mode may be damped less than they would be by physical viscous forces. These results suggest that definitive advice against using this method for DNS [7] may be premature.

Given the initial condition $\widehat{U}^0$, we consider the example to obtain the solution at the first time step $\widehat{U}^1$ using the classical fourth-order Runge–Kutta scheme. Besides minimizing the contribution of the spurious mode [4], this Runge-Kutta scheme also ensures that the order of accuracy used during initialization is not lower than that of the assumed AB method. This issue would arise, for example, if the Euler one-step method were used. The amplification factor $G^{RK4}$ of the Runge–Kutta scheme reads as

$$G^{RK4} = 1 + L^{Fo} + \frac{L^{Fo^2}}{2} + \frac{L^{Fo^3}}{6} + \frac{L^{Fo^4}}{24} \tag{34}$$

and it gives

$$\widehat{U}^1 = G^{RK4}\widehat{U}^0 \tag{35}$$

Then, beginning from the second time step, the solution can be computed using the total amplification factor of the AB method. It can be expressed as

$$\begin{aligned}\widehat{U}^2 &= \left[\alpha_{phys}G^{AB}_{phys} + \alpha_{spur}G^{AB}_{spur}\right]\widehat{U}^1 \\ &= \left[\alpha_{phys}G^{AB}_{phys} + \alpha_{spur}G^{AB}_{spur}\right]G^{RK4}\widehat{U}^0\end{aligned} \tag{36}$$

On the other hand, taking into account (24), one can equivalently state

$$\begin{aligned}\widehat{U}^2 &= \left(1 + \frac{3}{2}L^{Fo}\right)\widehat{U}^1 - \frac{1}{2}L^{Fo}\widehat{U}^0 \\ &= \left(1 + \frac{3}{2}L^{Fo}\right)G^{RK4}\widehat{U}^0 - \frac{1}{2}L^{Fo}\widehat{U}^0\end{aligned} \tag{37}$$

Equating (36) and (37) and using the property (33), leads to a set of two algebraic equations, from which the unknown fractions $\alpha_{phys}, \alpha_{spur}$ of the physical and spurious modes can be extracted. These fractions can be solved as

$$\alpha_{phys} = \frac{1 + \frac{3}{2}L^{Fo} - \frac{1}{2}\frac{L^{Fo}}{G^{RK4}} - G^{AB}_{spur}}{G^{AB}_{phys} - G^{AB}_{spur}} \tag{38}$$

$$\alpha_{spur} = -\frac{1 + \frac{3}{2}L^{Fo} - \frac{1}{2}\frac{L^{Fo}}{G^{RK4}} - G^{AB}_{phys}}{G^{AB}_{phys} - G^{AB}_{spur}} \tag{39}$$

The amplification factor (32) with the above weights is established for the second time step only. However, the overall stability of the method cannot be evaluated at such an early stage of the integration procedure, since the total amplification factor may vary between time steps, by variation of $\alpha_{phys}$ and $\alpha_{spur}$, eventually settling to a final form. In [4], for the midpoint leap-frog method applied to the convection equation, it was shown that the physical and spurious modes partially cancel each other for $n \geq 3$. It was further demonstrated that, at $n = 3$, the amplitudes of the physical and spurious modes are equal and remain unchanged during subsequent time steps. The interested reader is referred to Section 10.11 of [4] for further details. However, when diffusion is present, such partial cancellation and equalization of the mode amplitudes do not occur. If the physical and spurious modes are interpreted as two solution branches, as in [4], then each branch generates a pair of modes at every $n \geq 3$, and the amplitudes of these modes can vary. The same behaviour is postulated for the AB method analysed in the present work. In general, the total amplification factor at the $n^{th}$ time step can be expressed as

$$G^{AB,n}_{tot} = \alpha^n_{phys}G^{AB}_{phys} + \alpha^n_{spur}G^{AB}_{spur} \tag{40}$$

which is determined by the fractions of the physical and spurious modes in the $n^{th}$ time step. We note that $\alpha^n_{phys}$ and $\alpha^n_{spur}$ introduced above should not be interpreted as corresponding to the individual physical and spurious solution branches. Instead, they represent the fractions of the overall physical and spurious contributions to the solution. The iterative procedure that defines these fractions in all the steps, starting from the third one, reads as

$$\alpha^{n+1}_{phys} = \frac{1 + \frac{3}{2}L^{Fo} - \frac{1}{2}\frac{L^{Fo}}{G^{AB,n}_{tot}} - G^{AB}_{spur}}{G^{AB}_{phys} - G^{AB}_{spur}} \tag{41}$$

$$\alpha^{n+1}_{spur} = -\frac{1 + \frac{3}{2}L^{Fo} - \frac{1}{2}\frac{L^{Fo}}{G^{AB,n}_{tot}} - G^{AB}_{phys}}{G^{AB}_{phys} - G^{AB}_{spur}} \tag{42}$$

Taking the converged fractions of the physical and spurious modes calculated by the iterative scheme presented above allows determination of the total growth rate of the AB method, which, in turn, determines the scheme's stability boundary.

Analogous reasoning performed for the AM method leads to the following quadratic equation:

$$\left(1 - \frac{5}{12}L^{Fo}\right)\left(G^{AM}\right)^2 - \left(1 + \frac{8}{12}L^{Fo}\right)G^{AM} + \frac{1}{12}L^{Fo} = 0 \tag{43}$$

with two solutions

$$G^{AM}_{\pm} = \frac{1 + \frac{8}{12}L^{Fo} \pm \sqrt{\Delta}}{2\left(1 - \frac{5}{12}L^{Fo}\right)} \tag{44}$$

and the discriminant

$$\Delta = \left(1 + \frac{8}{12}L^{Fo}\right)^2 - \frac{1}{3}\left(1 - \frac{5}{12}L^{Fo}\right)L^{Fo} \tag{45}$$

$$= 1 + (kh)^2\left[\frac{7}{12}\left(N_c^2 + Pe^2(kh)^2\right) - Pe\right] + iN_c(kh)\left[\frac{7}{6}Pe(kh)^2 - 1\right]$$

Knowing that $L^{Fo} \to 0$ as $\Delta t \to 0$ leads to $G_+^{AM} \to 1$, and $G_-^{AM} \to 0$, and, similarly as for the AB method, we readily infer that $G_+^{AM} =: G_{phys}^{AM}$ is interpreted as the physical mode and $\widehat{G}_-^{AM} =: \widehat{G}_{spur}^{AM}$ is an additional spurious mode. Assuming that the first step of integration in time is performed with the RK4 scheme, the solution in the second time step with the AM method is expressed as

$$\widehat{U}^2 = \left[\alpha_{phys}G_{phys}^{AM} + \alpha_{spur}G_{spur}^{AM}\right]\widehat{U}^1 \tag{46}$$

$$= \left[\alpha_{phys}G_{phys}^{AM} + \alpha_{spur}G_{spur}^{AM}\right]G^{RK4}\widehat{U}^0 \tag{47}$$

On the other hand, taking into account (25), we have

$$\widehat{U}^2 = \frac{\left(1 + \frac{8}{12}L^{Fo}\right)\widehat{U^1} - \frac{1}{12}L^{Fo}U^0}{1 - \frac{5}{12}L^{Fo}} \tag{48}$$

$$= \frac{\left(1 + \frac{8}{12}L^{Fo}\right)G^{RK4} - \frac{1}{12}L^{Fo}}{1 - \frac{5}{12}L^{Fo}}U^0$$

Equating (46) and (48), while maintaining the property (33), the contribution of the physical and spurious modes can be expressed as

$$\alpha_{phys} = \frac{1 + \frac{8}{12}L^{Fo} - \frac{1}{12}\frac{L^{Fo}}{G^{RK4}} - G_{spur}^{AM}}{\left(1 - \frac{5}{12}L^{Fo}\right)\left(G_{phys}^{AM} - G_{spur}^{AM}\right)} \tag{49}$$

$$\alpha_{spur} = -\frac{1 + \frac{8}{12}L^{Fo} - \frac{1}{12}\frac{L^{Fo}}{G^{RK4}} - G_{phys}^{AM}}{\left(1 - \frac{5}{12}L^{Fo}\right)\left(G_{phys}^{AM} - G_{spur}^{AM}\right)} \tag{50}$$

Again, this result refers to the second time step. In analogy to (41)-(42), to obtain the fractions of the physical and spurious modes in consecutive steps, the recurrence procedure is applied. It reads as

$$\alpha_{phys}^{n+1} = \frac{1 + \frac{8}{12}L^{Fo} - \frac{1}{12}\frac{L^{Fo}}{G_{tot}^{AM,n}} - G_{spur}^{AM}}{\left(1 - \frac{5}{12}L^{Fo}\right)\left(G_{phys}^{AM} - G_{spur}^{AM}\right)} \tag{51}$$

$$\alpha_{spur}^{n+1} = -\frac{1 + \frac{8}{12}L^{Fo} - \frac{1}{12}\frac{L^{Fo}}{G_{tot}^{AM,n}} - G_{phys}^{AM}}{\left(1 - \frac{5}{12}L^{Fo}\right)\left(G_{phys}^{AM} - G_{spur}^{AM}\right)} \tag{52}$$

Having established the theoretical framework for the global spectral analysis, we investigate the spectral characteristics in the next section.

## 3. Spectral characteristics of Fourier-discretised convection-diffusion models

The framework of global spectral analysis discussed in the previous section will now be applied to investigate stability characteristics of the Adams-Bashforth method (Section 3.1). An explicit study of the evolution of a two-scale initial condition under AB will be presented in Section 3.2, while in Section 3.3 the origin of the spurious modes is elaborated upon. The analysis will be performed for a full range of CFL numbers ($N_c \in [0, \pi]$) for two previously selected Péclet numbers, $Pe = 0.01$ and $Pe = 0.05$ for which one can define a stable range of $N_c$. It will be shown that both situations are stable. Their stability characteristics manifest distinct qualitative differences. In a similar way, the Adams-Moulton method is analysed in Section 3.4.

### 3.1. Adams-Bashforth stability

As explained in the previous section, the three-level AB and AM methods require initialization with a two-level method, here RK4, which, based on the initial condition ($U(t^n = 0) = U^0$, $n = 0$), results in the solution at the time-step $n = 1$. The first time step when the AB method can be used is $n = 2$. The solution characteristic at $n = 2$, represented by the isolines of the total, physical, and spurious modes amplification factors for $Pe = 0.01$, is shown in Fig. 2. Note that the physical and spurious modes are multiplied by their weighting factors $\alpha_{phys}$ and $\alpha_{spur}$ calculated according to (38) and (39). The red line in the presented figures denotes the stability border for which $|G_{tot}^{AB}| = 1$. It is seen that within the stability region ($|G_{tot}^{AB}| \leq 1$), the solution is dominated by the physical mode, and only for $kh \to \pi$, a small fraction of the spurious mode may be discerned. Near the stability boundary, the spurious mode amplification factor reaches a magnitude of 0.05.

During the successive time steps, the stability characteristic changes due to the variability of $\alpha_{phys}$ and $\alpha_{spur}$ according to (41) and (42). To illustrate this process, the evolution of the amplification factors of the physical and spurious modes at $N_c = 0.2$ (stable region)

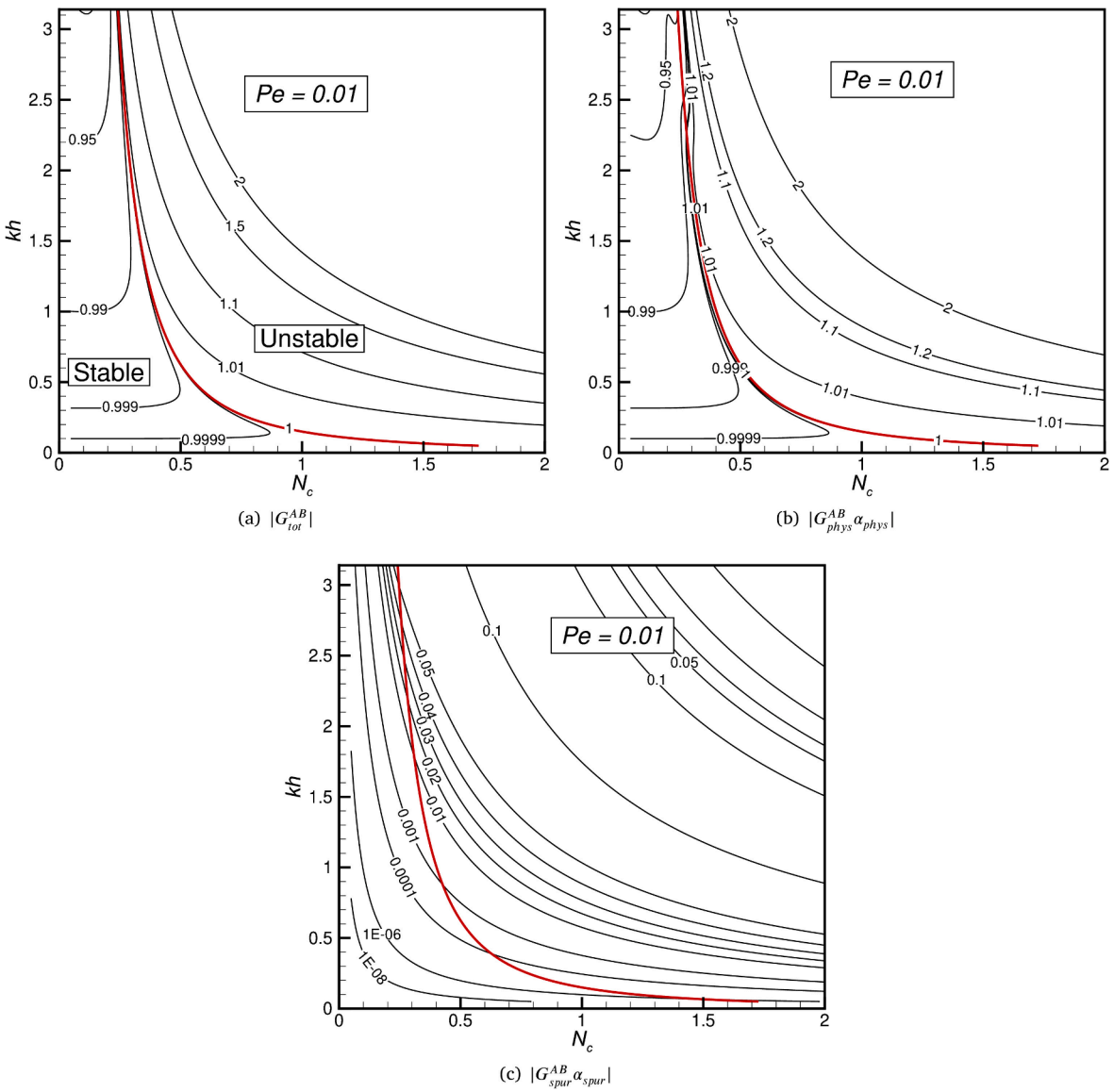


**Fig. 2.** Isolines of the total amplification factor (a) and its physical (b) and spurious (c) factors for $Pe = 0.01$. Results at the time-step $n = 2$. The red lines correspond to the modulus of the total amplification factor being equal to 1.

for $n = 3 - 10$ time steps is shown in Fig. 3. At $n = 3$, the amplification factor of the spurious mode in the range of the large scales (small $kh$) is virtually zero. In the medium- and small-scale range ($kh > \pi/2$), its values are no longer zero but remain significantly smaller than the physical mode amplification factor. Nevertheless, the spurious mode contribution cannot be neglected during the initial several time steps. This changes significantly as more time steps are taken. It can be seen that the amplification factor for the physical mode decreases by about 5% for the smallest scales, while the spurious mode amplification factor almost completely vanishes also at high $kh$, for $n = 10$, meaning that $G^{AB}_{tot} \approx \alpha_{phys} G_{phys}$ in the converged state.

Fig. 4 shows the total amplification factor with its physical and spurious fractions at ACS, i.e., when

$$\begin{aligned} \epsilon_\alpha &= |\alpha^{n+1}_{phys} - \alpha^{n}_{phys}| + |\alpha^{n+1}_{spur} - \alpha^{n}_{spur}| \\ &= 2|\alpha^{n+1}_{phys} - \alpha^{n}_{phys}| < 10^{-6} \end{aligned} \tag{53}$$

The red line in Fig. 4a shows the previously obtained stability border at time step $n = 2$, while the blue line denotes the asymptotic stability border. It can be seen that in the range of low $kh$, the stable region expands to slightly larger $N_c$, while it narrows when $kh \to \pi$. Noting that the solution stability is determined by $|G^{AB}_{tot}| = 1$ for which $N_c$ is the smallest, it can be concluded that the stability region at the converged state is somewhat smaller compared to the usually adhered to estimate at $n = 2$. Nevertheless, it is still determined by the physical mode fraction, whose distribution changes only slightly (see Fig. 4b). The most pronounced differences

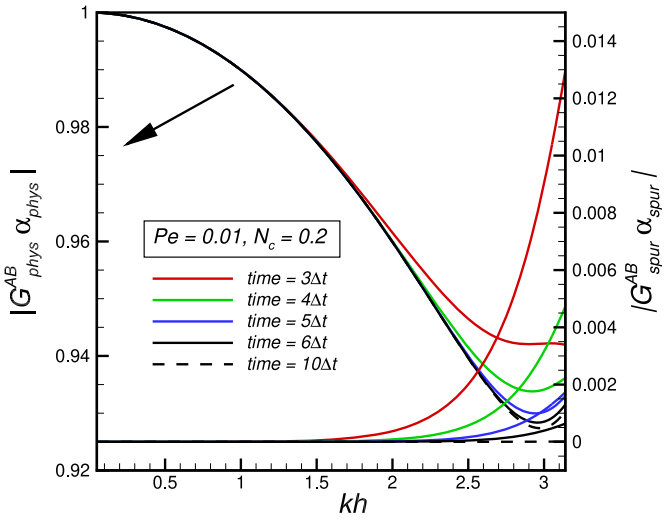


**Fig. 3.** Evolution of the physical and spurious modes for $n = 3 - 10$ time steps ($n\Delta t$) for $Pe = 0.01$ and $N_c = 0.2$. The arrow indicates the vertical axis corresponding to the group of lines.

are found for the spurious mode fraction shown in Fig. 4c. While for $n = 2$ its largest values within the stability region reach 0.5, in the converged state they are lower than the assumed convergence tolerance $\epsilon$ (53). We note that decreasing $\epsilon$ reduces the spurious mode's contribution until it eventually becomes dominated by round-off error. Thus, for $Pe = 0.01$, the influence of the spurious mode is negligible.

The stability characteristics discussed above change significantly for $Pe = 0.05$. Fig. 5 shows the total amplification factor along with its physical and spurious modes, computed at time step $n = 2$ (left column) and at ACS (right column). Compared to the solution for $Pe = 0.01$, the position of the stability border ($|G^{AB}_{tot}| = 1$) and the values of $|G^{AB}_{tot}|$ on both sides of this border are similar. A small island of the stability region appears at $n = 2$ near $kh = \pi$, originating from the spurious contribution to $G^{AB}_{tot}$ that results from applying the RK4 method at the first time step. It disappears in subsequent steps and therefore has no influence on the stability at ACS. One can observe that the shift of the stability boundary (blue line) relative to its position at $n = 2$ is noticeably larger than the corresponding change found for $Pe = 0.01$. Over a wide range of $kh$, the boundary shifts significantly toward lower $N_c$. Based on the stability map for $n = 2$, one would choose the critical CFL number as $N_{c,stab} = 0.3575$, whereas in ACS it decreases significantly to $N_{c,stab} = 0.2475$. Later, in Section 3.3, we will show that long-term computations performed with $N_c$ slightly larger than this value indeed become unstable.

A striking difference, compared to the case with $Pe = 0.01$, is found in the distributions of the physical and spurious modes. The discontinuity at $kh = \sqrt{2/(9Pe)} \approx 2.108$, observed for $|G^{AB}_{phys,spur}|$ in Fig. 1, appears also for $|\alpha_{phys,spur} G^{AB}_{phys,spur}|$ which extends into the stable region. As discussed in the previous section, when crossing the discontinuity line from below, the physical mode decreases while the spurious mode increases. In fact, the overall variation of $|G^{AB}_{tot}|$ is smooth both at $n = 2$ and at the converged state. At $n = 2$, the physical and spurious contributions to $|G^{AB}_{tot}|$ are not negligible in almost the entire $kh - N_c$ plane. The situation changes in the converged state, where the physical mode above (below) the discontinuity becomes nearly zero (of order one or higher), with the opposite trend observed for the spurious mode. This indicates that, as $\alpha_{phys}$ and $\alpha_{spur}$ converge toward ACS, either the physical or spurious contribution to $G^{AB}_{tot}$ vanishes, and this happens abruptly at the discontinuity line. We note that the reason for that is not because $G^{AB}_{phys}$ or $G^{AB}_{spur}$ approach zero, as they have the values defined by (29), but due to either $\alpha_{phys}$ or $\alpha_{spur}$ converging to one. Under the imposed condition $\alpha_{phys} + \alpha_{spur} = 1$ this results in the vanishing of $|G^{AB}_{phys}\alpha_{phys}|$ or $|G^{AB}{}_{spur}\alpha_{spur}|$, depending on the precise local situation in the stability map.

Fig. 6 presents a zoomed view of a region where the discontinuity line (green) extends into the stability region and reaches the point P where $|G^{AB}_{phys}| = |G^{AB}{}_{spur}|$ (see Fig. 1). From there, it goes up to $kh = \pi$ almost parallel to the line $|G^{AB}_{tot}| = 1$. At a set of discrete points, the green line marks locations between the grid points, i.e., where $\alpha_{phys}$ and $\alpha_{spur}$ are both equal to 0.5. The grey color denotes the part of the stable region where $\alpha_{spur} = 1,\ \alpha_{phys} = 0$. Two important observations can be made based on these results. First, unlike for $Pe = 0.01$, the stability limit for $Pe = 0.05$ is determined by the spurious mode contribution. The second point concerns the selection of $\alpha_{spur},\ \alpha_{phys}$ as zero or one in the converged state. In the grey region and everywhere above the discontinuity lines, we observe that $|G^{AB}_{spur}| > |G^{AB}_{phys}|$ with $\alpha_{spur} = 1,\ \alpha_{phys} = 0$, while the opposite holds to the left of and below the discontinuity line ($|G^{AB}_{spur}| < |G^{AB}_{phys}|$ leading to $\alpha_{spur} = 0,\ \alpha_{phys} = 1$). Hence, we infer that during the iterative procedure (41)–(42), either $\alpha_{spur}$ or $\alpha_{phys}$ converges to 1, at which point the corresponding amplification factor (29) is larger than the other. In fact, $|G^{AB}_{tot}|$ in ACS is defined as

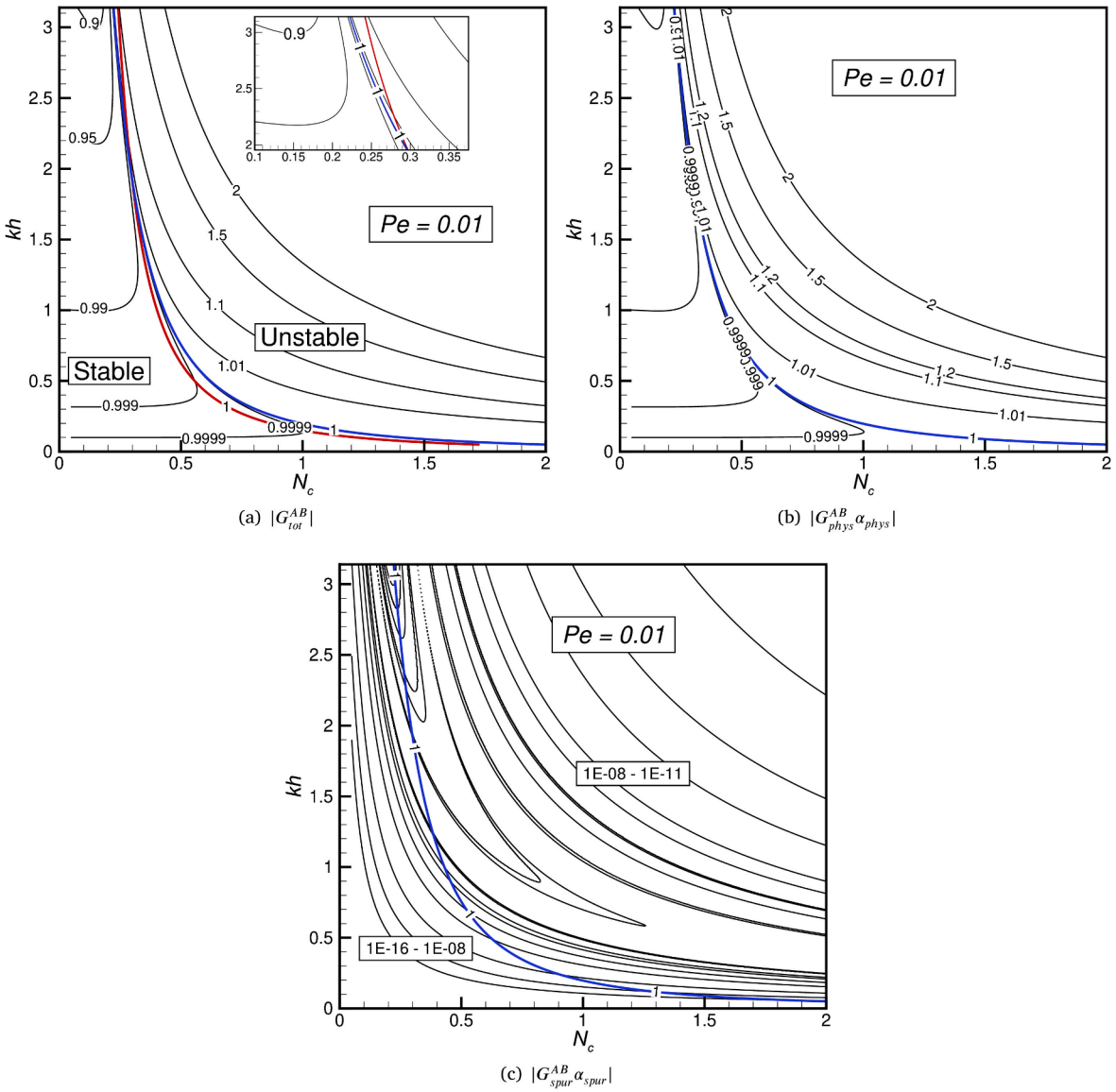


**Fig. 4.** Isolines of the total amplification factor (a) and its physical (b) and spurious (c) mode factors for $Pe = 0.01$ at ACS. Red line - the stability border at $n = 2$, blue line in all subfigures - the stability border at ACS.

the maximum of the two amplification factors, i.e.,

$$|G^{AB}_{tot}| = \begin{cases} |G^{AB}_{phys}|, & \text{if } |G^{AB}_{phys}| > |G^{AB}_{spur}| \\ |G^{AB}_{spur}|, & \text{otherwise.} \end{cases} \tag{54}$$

Thus, the stability condition for $|G^{AB}_{tot}| \leq 1$ defining $N_{c,stab}$ reduces exactly to the Dahlquist stability theorem [18], which assures stability of a general $k$-level method by requiring $\max_k(|G_k|) \leq 1$. In the present case this leads to $\max(|G^{AB}_{phys}|, |G^{AB}_{spur}|) \leq 1$. Fig. 7 shows the evolution of $|G^{AB}_{phys}\alpha_{phys}|$ and $|G^{AB}_{spur}\alpha_{spur}|$ toward the converged state at $N_c = 0.2$ (dashed line crossing the grey region in Fig. 6). In contrast to their monotonic decrease observed for $Pe = 0.01$ (see Fig. 3), for $Pe = 0.05$ both $|G^{AB}_{phys}\alpha_{phys}|$ and $|G^{AB}{}_{spur}\alpha_{spur}|$ vary significantly over the subsequent time steps, and the convergence process is also significantly longer. In the converged state, the abrupt emergence of the spurious mode is accompanied by the simultaneous disappearance of the physical mode, as discussed above. This occurs at $kh \approx 2.75$, corresponding to the point where the dashed line intersects the discontinuity line in Fig. 6. For $kh > 2.75$, the variability of $|G^{AB}_{spur}\alpha_{spur}|$ arises from the dependence of $G^{AB}_{spur}$ on $kh$ (see Eq. (29) and Fig. 1).

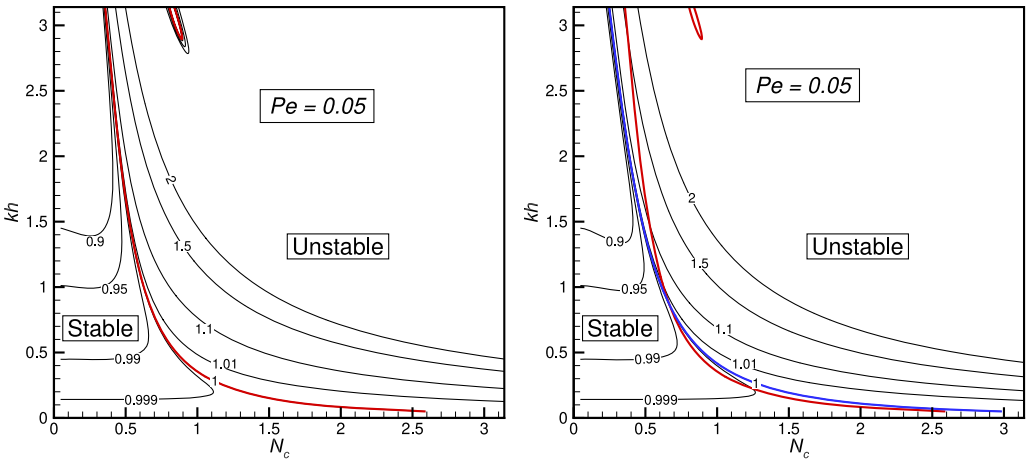


(a) $|G^{AB}_{tot}|$ at $n = 2$ (left) and at the converged state (right)

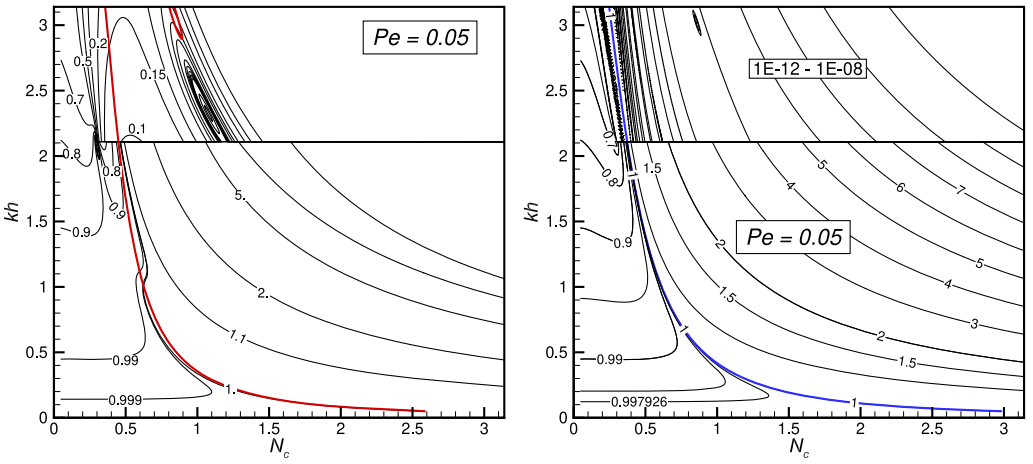


(b) $|G^{AB}_{phys}\alpha_{phys}|$ at $n = 2$ (left) and at the converged state (right)

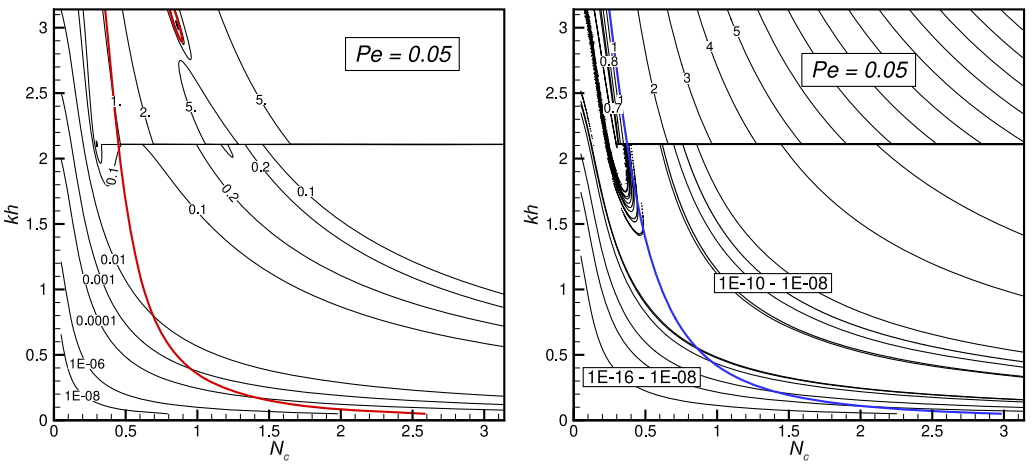


(c) $|G^{AB}_{spur}\alpha_{spur}|$ at $n = 2$ (left) and at the converged state (right)

**Fig. 5.** Isolines of the total amplification factor (a) with its physical (b) and spurious (c) mode factors at $Pe = 0.05$. Results at the time step $n = 2$ (left column) and at the converged state (right column). Red line - the stability border at $n = 2$, blue line - the stability border at ACS. (For interpretation of the references to colour in this figure legend, the reader is referred to the web version of this article.)

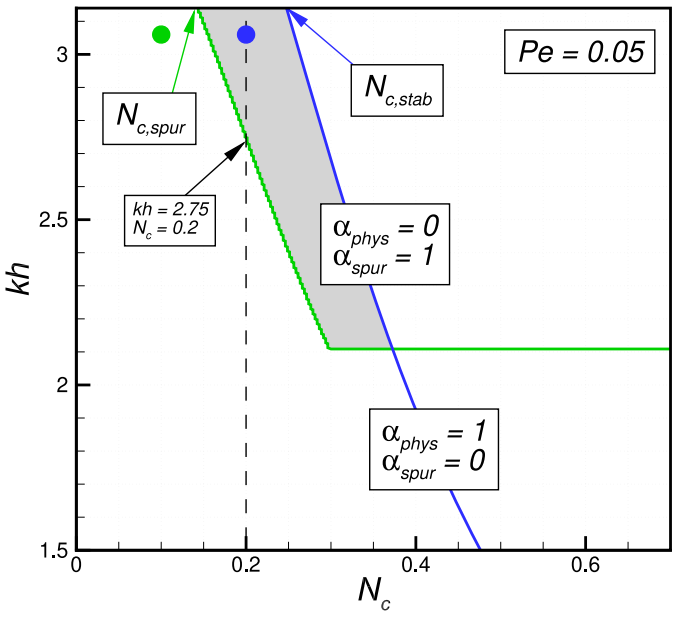


**Fig. 6.** Regions of the physical and spurious mode occurrence for $Pe = 0.05$. Grey color represents the part of the stability region determined by $G^{AB}_{spur}$. Green and blue dots show the locations of the high-frequency modes of a bi-modal initial function analyzed in Section 3.2.

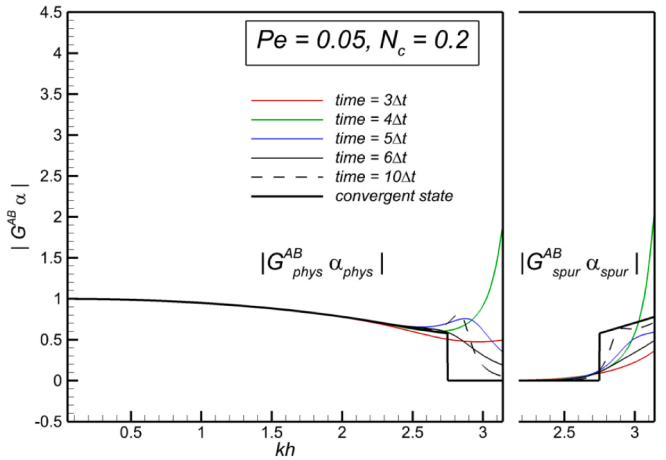


**Fig. 7.** Evolution of the physical (left) and spurious (right) mode for $n = 3 - 10$ time steps ($n\Delta t$) and the converged state for $Pe = 0.05$ and $N_c = 0.2$.

The next section demonstrates that performing computations starting from an initial condition containing a high-frequency length scale and an $N_c$ value for which $G^{AB}_{tot}$ lies within the grey region in Fig. 6 results in nonphysical oscillations that persist over a long simulation time. From Fig. 6, however, it can be inferred that this situation can be avoided by selecting a sufficiently low $N_c$, thereby eliminating the contribution of the spurious mode altogether. Let us call this critical CFL number $N_{c,spur}$, understood as the value of $N_c$ at which the discontinuity line intersects the horizontal line $kh = \pi$, as indicated by the green arrow in Fig. 6. Hence, the stability region can be divided into two parts: $0 < N_c < N_{c,spur}$, in which the solution is determined solely by the physical mode, and $N_{c,spur} < N_c < N_{c,stab}$, where the evolution of high-frequency scales is entirely governed by the spurious mode contribution to $G^{AB}_{tot}$, followed by the unstable region for $N_c > N_{c,stab}$.

### 3.2. Results for a bi-modal initial condition

This section clarifies the differences in the solution between a pure physical mode and a mixed physical-spurious regime at $Pe = 0.05$. We analyze the evolution of the bi-modal function defined as

$$u(x,t) = A_1(t)\sin\left(k_1(x-ct)\right) + A_2(t)\sin\left(k_2(x-ct)\right) \tag{55}$$

where $k_{1,2}$ denote the wavenumbers and $A_{1,2}(t) = A_{1,2}\exp\left(-\nu k_{1,2}^2 t\right)$ are the amplitudes of the components with $A_{1,2}$ assumed to be their initial values. The computational domain has length $L = 2\pi$, and the numerical mesh consists of $N = 2K + 1$ grid points, where $K = 256$ is the number of Fourier modes. On this mesh, we consider $k_1 = 10$ ($k_1\ h = 0.1225$) and $k_2 = 250$ ($k_2\ h = 3.06$) as the representative low- and high-frequency modes. In the following discussion, for brevity, we refer to them as the $k_1$ and $k_2$ modes, respectively. The amplitudes are set to $A_1 = 1$ and $A_2 = 10^7$. The rationale for choosing a large value of $A_2$ is the proportionality $A_2(t) \propto \exp(-k^2)$, which leads to rapid damping of the high-frequency component. In the analyzed example, if $A_2$ is small, $A_2(t)$ decays to zero before $G_{tot}^{AB}$ reaches ACS, not allowing the impact of the spurious mode on the solution to be observed.

The computations are carried out for two CFL numbers, $N_c = 0.1$ and $N_c = 0.2$, which, together with the assumed values of $k_{1,2}h$, determine the locations of the modes at specific points in the stability diagram. In Fig. 6, the $k_2$ mode is represented by the green and blue dots. The green dot, corresponding to $N_c = 0.1$, lies within the range $N_c < N_{c,spur}$, while the blue one for $N_c = 0.2$ lies in $N_{c,spur} < N_c < N_{c,stab}$, i.e., in the stability region governed by the spurious mode. Its value at the specific location is relatively large, $|G^{AB}{}_{spur}| = 0.737$. The time step used in the simulation is constant, $\Delta t = 10^{-4}$. The convection velocity and diffusion coefficient are computed as $c = N_c\, h/\Delta t$ and $\nu = Pe\, h^2/\Delta t$, respectively.

Fig. 8 shows the analytical and numerical profiles of $u(x)$ after $50\Delta t$ and a solution error calculated as $u_{\text{exact}}(x) - u_{\text{num.}}(x)$. It can be noted that, due to the dependence of the convection velocity on $N_c$, the evolution of the initial profiles is not identical. This difference, however, has no impact on the solution's stability characteristics. It can be seen that for $N_c = 0.1$, the numerical solution agrees very well with the analytical one. The existing tiny differences are imperceptible to the naked eye. The solution error is approximately two orders of magnitude lower than for $N_c = 0.2$. In this case, the error is large and manifests as high-frequency oscillations with local amplitudes significantly above the analytical value. Note that the long-wave oscillation of the maxima and minima of the solution and the error, observed for both $N_c$, is not the effect of the generation of an additional mode but originates from the marginal sampling resolution of the $k_2$ mode.

Fig. 9 shows comparisons of the amplitudes calculated numerically ($A_{1,num}(t)$ and $A_{2,num}(t)$) with their analytical counterparts. It can be seen that these follow closely only when $N_c = 0.1$, for which $A_{1,2,num}(t)$ decreases exponentially, with the slope in the log–lin plot almost coinciding $-\nu k_{1,2}^2$. At the end of the simulation, the ratios $A_{1,num}(t)/A_1(t) = 0.9999$ and $A_{2,num}(t)/A_2(t) = 0.8735$ indicate that $\nu_{num}(k_1) \approx \nu$ and $\nu_{num}(k_2) > \nu$. For $N_c = 0.2$, the amplitude $A_{1,num}(t)$ is predicted almost as accurately as for $N_c = 0.1$, with the blue and red lines virtually overlapping. Significant discrepancies, however, are observed for $A_{2,num}(t)$. These appear not only at the initial time ($t < 10^{-3}$), where $A_{2,num}(t)$ oscillates due to the variability of $|G_{phys}^{AB}\alpha_{phys}|$ and $|G_{spur}^{AB}\alpha_{spur}|$ (see Fig. 7), but also at later times, where it decreases evidently too slowly. At $t = 50\Delta t$, $A_{1,num}(t)/A_1(t) = 0.9999$ ($\nu_{num}(k_1) \approx \nu$), but $A_{2,num}(t)/A_2(t) = 732.1$, which means significantly smaller damping resulting from $\nu_{num}(k_2) < \nu$.

From Fig. 9, it can be seen that after the initial fluctuations, $A_{2,num}(t)$ follows an exponential decay. In general, one can write $A_{num}(t) = A\exp\left(-\nu_{num}(t), k^2, t\right)$, from which an instantaneous ratio $\nu_{num}(t)/\nu$ can be calculated as

$$\frac{\nu_{num}(t)}{\nu} = -\frac{\ln(A_{num}(t)/A)}{\nu\, k^2\, t} \tag{56}$$

Fig. 10 presents $\nu_{num}(t)/\nu$ for $k_{1,2}$ modes and both $N_c$. First, it can be seen that in all cases, $\nu_{num}(t)$ varies not only at the beginning, as one might expect based on $A_{2,num}(t)$, but throughout the entire simulation. The reason for that is the long convergence process of $G_{phys}^{AB}\alpha_{phys}$ and $G_{spur}^{AB}\alpha_{spur}$. The rate at which $\nu_{num}(t)$ approaches a plateau differs significantly depending on $k$ and $N_c$, and is the slowest for the $k_2$ mode at $N_c = 0.2$ due to strong variations of $|G_{phys}^{AB}\alpha_{phys}|$ and $|G_{spur}^{AB}\alpha_{spur}|$ (see Fig. 7). However, in all cases $\nu_{num}(t)/\nu$ ultimately tends to a constant value at ACS. GSA allows for finding it from (17) without the need for performing a numerical experiment as done above. Moreover, it enables decomposing $\nu_{num}(t)/\nu$ into the physical and spurious contributions, both during the transient phase and at the converged state. In this case, $\nu_{num,phys}(t)/\nu$ and $\nu_{num,spur}(t)/\nu$ are calculated from one of the two following expressions

$$\frac{\nu_{num}}{\nu} = \begin{cases} -\dfrac{\ln\left(\left|G_{phys}^{AB}\right|\right)}{Pe\left(kh\right)^2}, & \text{if } \alpha_{phys} = 1, \alpha_{spur} = 0 \\ -\dfrac{\ln\left(\left|G_{spur}^{AB}\right|\right)}{Pe\left(kh\right)^2}, & \text{otherwise} \end{cases} \tag{57}$$

Performing such a decomposition for the numerical phase speed (16) and the group velocity (19), one can separately represent them on the $kh - N_c$ plane in a similar way as the physical and spurious parts of the amplification factor. Fig. 11 shows the isolines of the physical part of the numerical diffusion coefficient, the numerical phase speed ($c_{num,phys}/c$), and the group velocity ($V_{g,num,phys}/V_{g,phys}$) at ACS. As shown, for sufficiently small values of $kh$, these parameters remain close to their exact counterparts. The bold pink line in Fig. 11a, corresponding to $\nu_{num,phys}/\nu = 1$, divides the stable region into two parts: on the left side, the numerical solution exhibits similar damping as the physical solution, whereas on the right side it shows weaker damping. In the latter case, $\nu_{num,phys}/\nu \to 0$ as the stability limit is approached and becomes negative upon crossing it.

As wave numbers increase and remain within the stability region, the correspondence between numerical and physical parameters becomes less precise. For $kh > 2$, $\nu_{num,phys}/\nu$ varies in the range $1.0 - 1.2$ meaning excessive numerical dissipation. Simultaneously, $c_{num,phys}/c$ varies from 0.7 to 0.9, whereas $V_{g,num,phys}/c$ locally approaches zero and becomes negative when $kh \to \pi$. This would imply slower motion of high-frequency waves, with their envelopes moving in the opposite direction. A similar set of plots showing the spurious-mode contribution to the numerical diffusion coefficient ($\nu_{num,spur}/\nu$), numerical phase speed ($c_{num,spur}/c$), and group velocity ($V_{g,num,spur}/V_{g,phys}$) is presented in Fig. 12. It can be seen that the distributions of these quantities differ significantly from those corresponding to the physical mode. In the region between the stability and discontinuity lines $\nu_{num,spur}/\nu$ is locally much

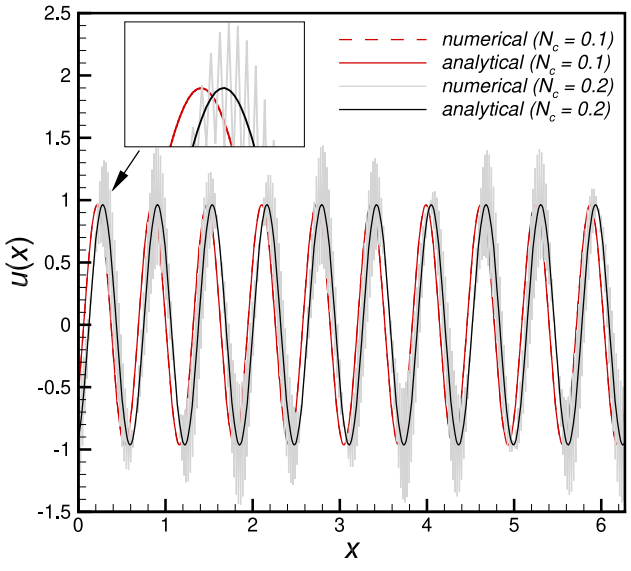


(a)

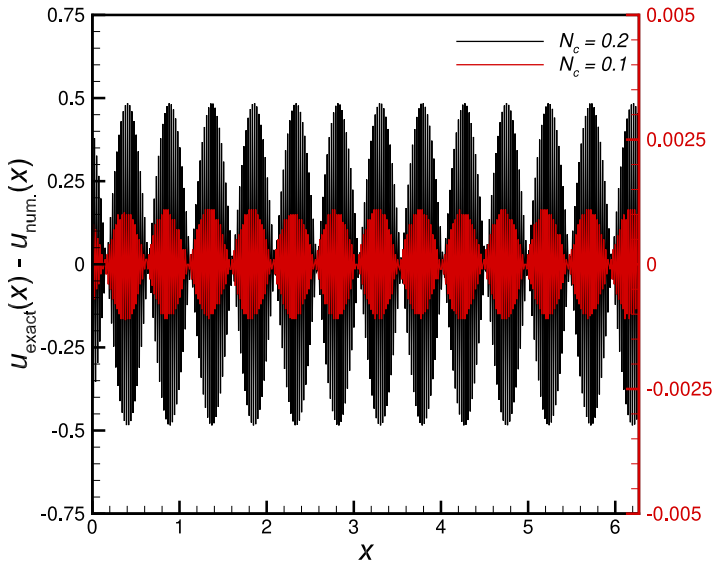


(b)

**Fig. 8.** Analytical and numerical solution (AB method) for $N_c = 0.1$ and $N_c = 0.2$ at $Pe = 0.05$ for $t = 50\Delta t$ (a) and the solution error (b).

smaller than one, resulting in insufficient damping of the $k_2$ mode. Moreover, as $c_{num,spur}/c > 1$, it propagates faster. Table 1 lists the exact values of the physical and spurious parts of $\nu_{num}$, $c_{num}$, and $V_{g,num}$ at the locations corresponding to $k_1 h$ and $k_2 h$ for $N_c = 0.1$ and $N_c = 0.2$. From these data, one can infer that, as the simulation proceeds, both the amplitude and position of the $k_1$ mode will remain close to the analytical values over a relatively long time. For the $k_2$ mode at $N_c = 0.1$, the discrepancies in $V_{g,num}$ and $c_{num}$ are substantial. The resulting error, however, is masked by the accurately predicted position of the $k_1$ mode, whose amplitude at $50\Delta t$ remains large. Additionally, the influence of the negative group velocity cannot be observed for an isolated mode. At $N_c = 0.2$, due to the significantly smaller $\nu_{num}$ and an almost threefold increase in $c_{num}$, the amplitude of the $k_2$ mode decays slower than in the analytical solution, while its position advances ahead of it.

### 3.3. Spurious mode origin

The physical and spurious modes are inherently tied to the nature of the AB method and arise as the two solutions of the corresponding quadratic Eq. (29). However, the observed dominant role (54) of one mode over the other at the converged state cannot

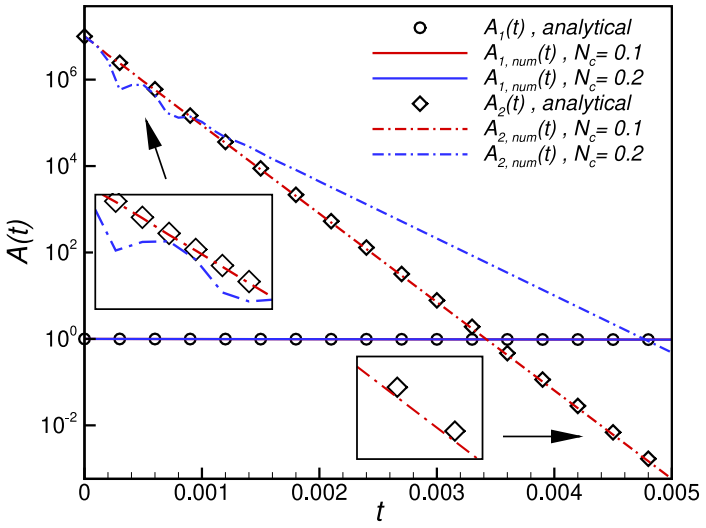


**Fig. 9.** Evolution of the amplitudes of the bi-modal function (55) for $N_c = 0.1$ and $N_c = 0.2$ at $Pe = 0.05$.

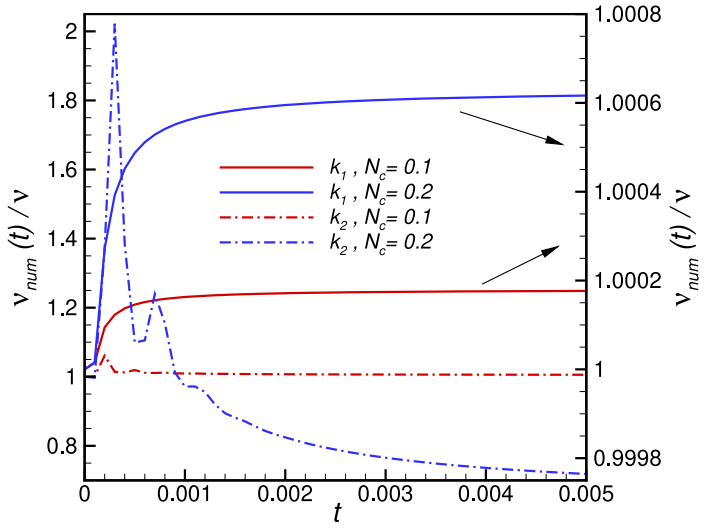


**Fig. 10.** Evolution of the numerical diffusion coefficient of the bi-modal function (55) for $N_c = 0.1$ and $N_c = 0.2$ at $Pe = 0.05$.

be assessed a priori, as it results from the iterative procedure (41)-(42). This appears to be triggered by the bootstrapping, where the two-time-level RK4 method is used to obtain the solution at $n = 1$. The impact of the time-integration method used in the initial step has been analyzed, among others, in [4]. For the leap-frog method initialized with either the explicit Euler or the RK4 method, it was shown that the RK4 initialization leads to a significantly smaller spurious-mode amplification factor at the later time steps. In the present case, the amplification factor produced by the RK4 initialization differs significantly from the physical mode of the AB method employed in the subsequent time steps. This discrepancy between the amplification factors could be the primary source of the local dominance of the spurious mode. It can be shown that if in Eqs. (38) and (39) instead of the amplification factor for the RK4 method, the amplification factor of the physical mode of the AB method itself is applied, the weighting factors are $\alpha_{phys} = 1$ and $\alpha_{spur} = 0$, respectively. *This raises a critical question: is it possible to completely eliminate spurious modes by a proper initialization using the solution at the first time-step generated by the integration method actually used?* In the case of periodic problems under consideration, such an approach is straightforward. The Fourier transform of the initial condition is multiplied by the physical mode known from GSA, and the inverse transform leads to the solution for the first step. Further time steps are performed in the physical space. Numerical examples of such an approach will be discussed later. However, the assumption that the first step of the calculations is performed using only the physical amplification factor is questionable in practice due to round-off errors. More likely is the assumption that a certain marginal level of the spurious mode may initially appear and influence its later evolution. To analyze this issue, we consider two cases. We set $\alpha_{spur} = 0$, corresponding to a perfect initialization through the AB method at $n = 1$, and $\alpha_{spur} = 10^{-8}$ to mimic a deviation from this state. The iterative procedure (41)-(42) is then continued until ACS is obtained. Fig. 13a and b show the results

**Table 1**
Physical and spurious fractions of $\nu_{num}$, $c_{num}$ and $V_{g,num}$ for the bi-modal function ($k_1 = 10$, ($k_1 h = 0.1225$) and $k_2 = 250$, ($k_2 h = 3.0619$)) for $Pe = 0.05$ at ACS.

| | $N_c = 0.1$ | | $N_c = 0.2$ | |
|---|---|---|---|---|
| | $k_1$ | $k_2$ | $k_1$ | $k_2$ |
| $\nu_{num,phys}/\nu$ | 1.00018 | 1.00479 | 1.00063 | 0.0 |
| $\nu_{num,spur}/\nu$ | 0.0 | 0.0 | 0.0 | 0.6481 |
| $c_{num,phys}/c$ | 1.00006 | 0.7249 | 1.00025 | 0.0 |
| $c_{num,spur}/c$ | 0.0 | 0.0 | 0.0 | 2.9770 |
| $V_{g,num,phys}/c$ | 1.00018 | −0.3090 | 1.00075 | 0.0 |
| $V_{g,num,spur}/c$ | 0.0 | 0.0 | 0.0 | 1.7027 |

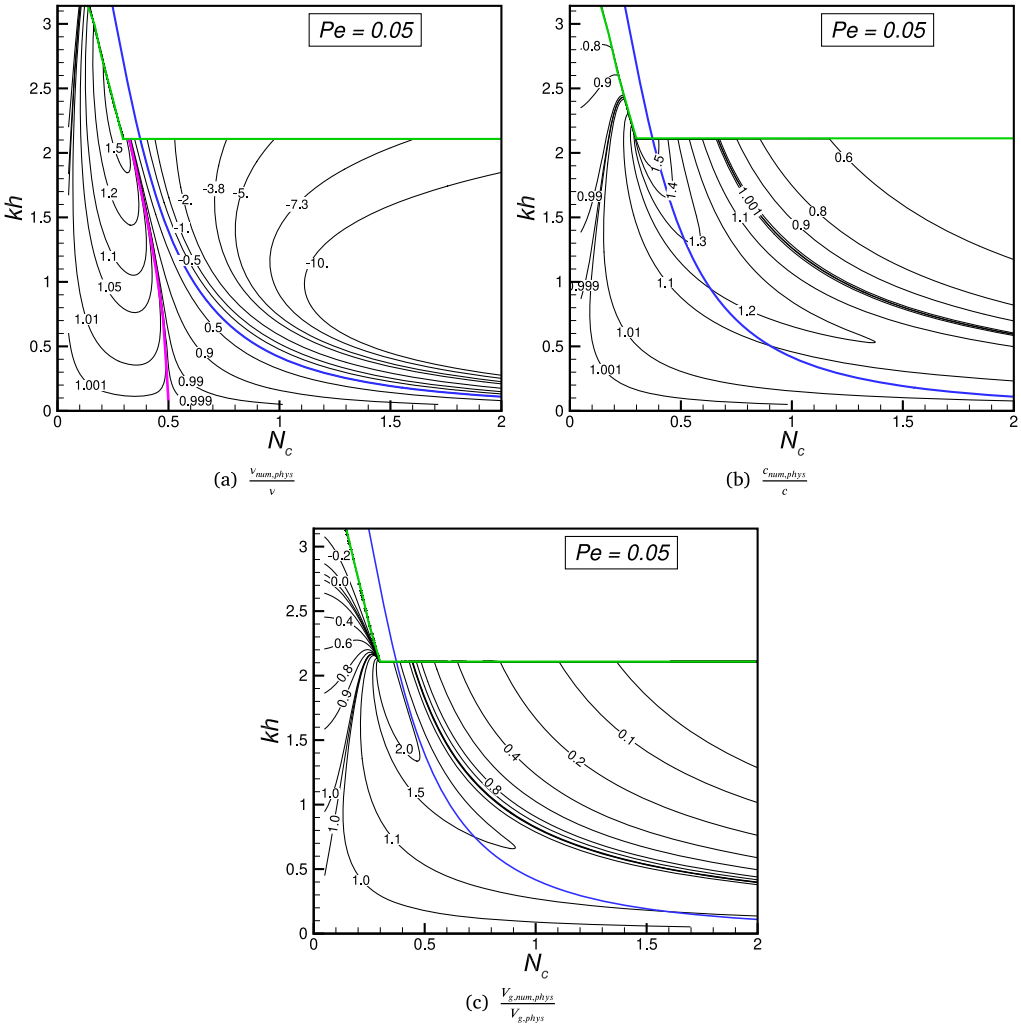


**Fig. 11.** Isolines of the physical contribution to the numerical diffusion coefficient (a), phase speed (b), group velocity for the AB scheme at ACS for $Pe = 0.05$. Green line - the discontinuity line, blue line - the stability border at ACS, pink line - the border between regions of the numerical viscosity smaller and higher than the physical viscosity.

for the asymptotic distribution of the physical and spurious modes iterated from the initial condition, at $\alpha_{spur} = 0$. It can be seen that at the chosen convergence level, only the physical mode is present in ACS, and the spurious mode does not emerge. As a result, we obtain 'numerical noise' at the level of machine accuracy alone, which does not show monotonic isocontours but a scatter of points. In contrast, the results obtained for $\alpha_{spur} = 10^{-8}$, presented in Fig. 13c and d, clearly show the emergence of the spurious mode, and for this case the isocontour $|G_{tot}^{AB}| = 1$ almost perfectly coincides with that shown in Fig. 5. It follows that the choice of the method applied at the first step affects the stability map during the beginning of the time integration, but does not alter its overall character-

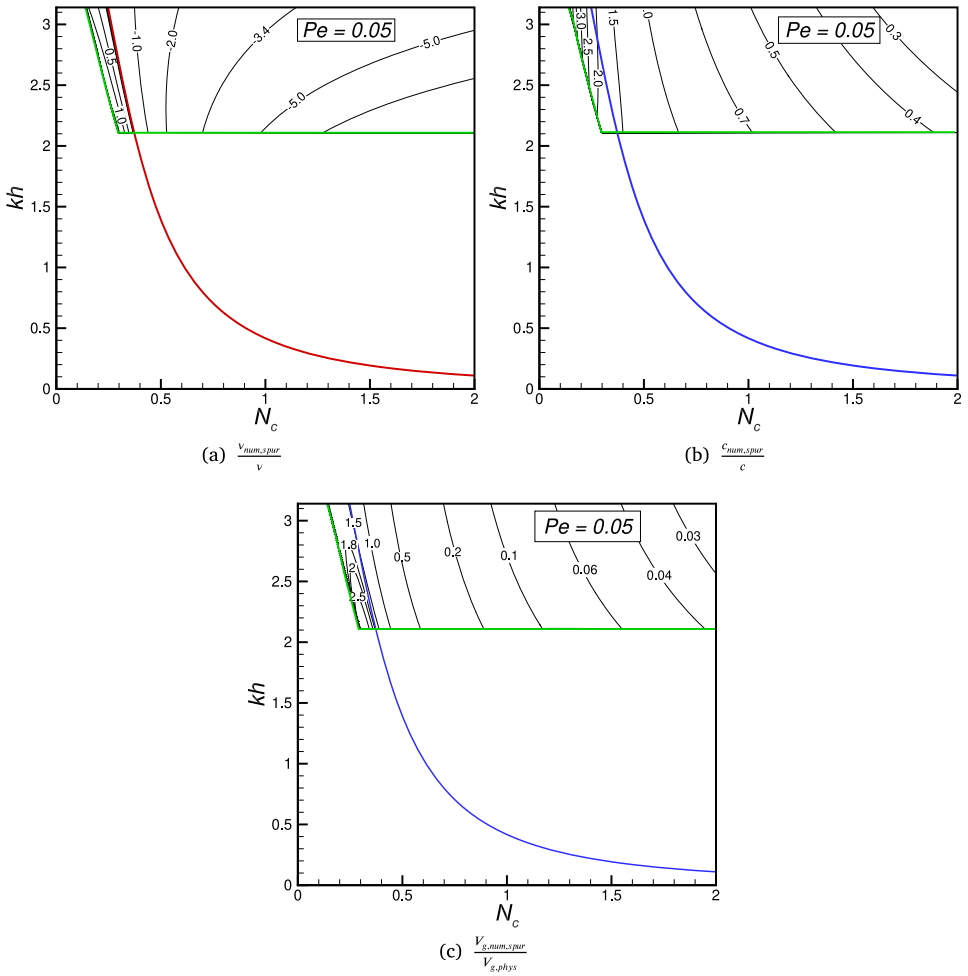


**Fig. 12.** Isolines of the spurious contribution to the numerical diffusion coefficient (a), phase speed (b), group velocity for the AB scheme at ACS for $Pe = 0.05$. Green line - the discontinuity line, blue line - the stability border at ACS. (For interpretation of the references to colour in this figure legend, the reader is referred to the web version of this article.)

istics at ACS. We also note that, for the initialization with $\alpha_{spur} = 0$, when the computations are continued for a very long time, the final distribution matches that obtained for the initialization with $\alpha_{spur} = 10^{-8}$.

The above analysis shows that avoiding the spurious mode for certain values of $Pe - N_c$ is impossible. To further underpin this, the following computations are performed. We consider a multi-modal function defined as

$$u(x,t) = \sum_{k=0}^{K} A_k(t) \sin\left(k(x - ct)\right) \tag{58}$$

with $A_k(t) = A_k \exp\left(-\nu k^2 t\right)$. As in the previous test case, the computational domain is $L = 2\pi$, and the numerical mesh consists of $N = 2K + 1$ grid points with $K = 256$ representing the number of Fourier modes. The initial amplitude of all modes is set to $A_k(t = 0) = A_k = 1$. The time step is $\Delta t = 10^{-4}$ and the simulations are performed for two CFL numbers $N_c = 0.245$ and $N_c = 0.25$. Along with the assumed $Pe = 0.05$ they are used to compute the convection velocity and viscosity ($c$, $\nu$). Two initialization methods are considered for the first time step: RK4 and AB. In the latter case, the earlier-mentioned procedure employing the Fourier transform of the initial condition is applied without any purposely added disturbance. We note that for $N_c = 0.245$ the solution evolves in time with the spurious mode ($|G^{AB}_{tot}| = |G^{AB}_{spur}\alpha_{spur}|$, see Fig. 6) but it should be stable regardless of the initialization method as for $Pe = 0.05$ the stability limit is $N_{c,stab} = 0.2475$. For $N_c = 0.25$, the situation is different, and the following scenarios are possible:

1. in case of initialization by the RK4 method, the solution is stable over some time during which the stability limit shifts from $N_{c,stab} = 0.3575$ set at $n = 1$ (see Fig. 5a and corresponding discussion) to $N_{c,stab} = 0.2475$ at ACS;
2. in case of the initialization by the AB method the solution is: (a) stable over the infinite simulation time as the spurious mode does not occur and for $N_c = 0.25$ we have $|G^{AB}_{tot}| = |G^{AB}_{phys}\alpha_{phys}| < 1$ for all $kh$-modes (see Fig. 13a); (b) unstable as in the case 1) if the spurious mode appears.

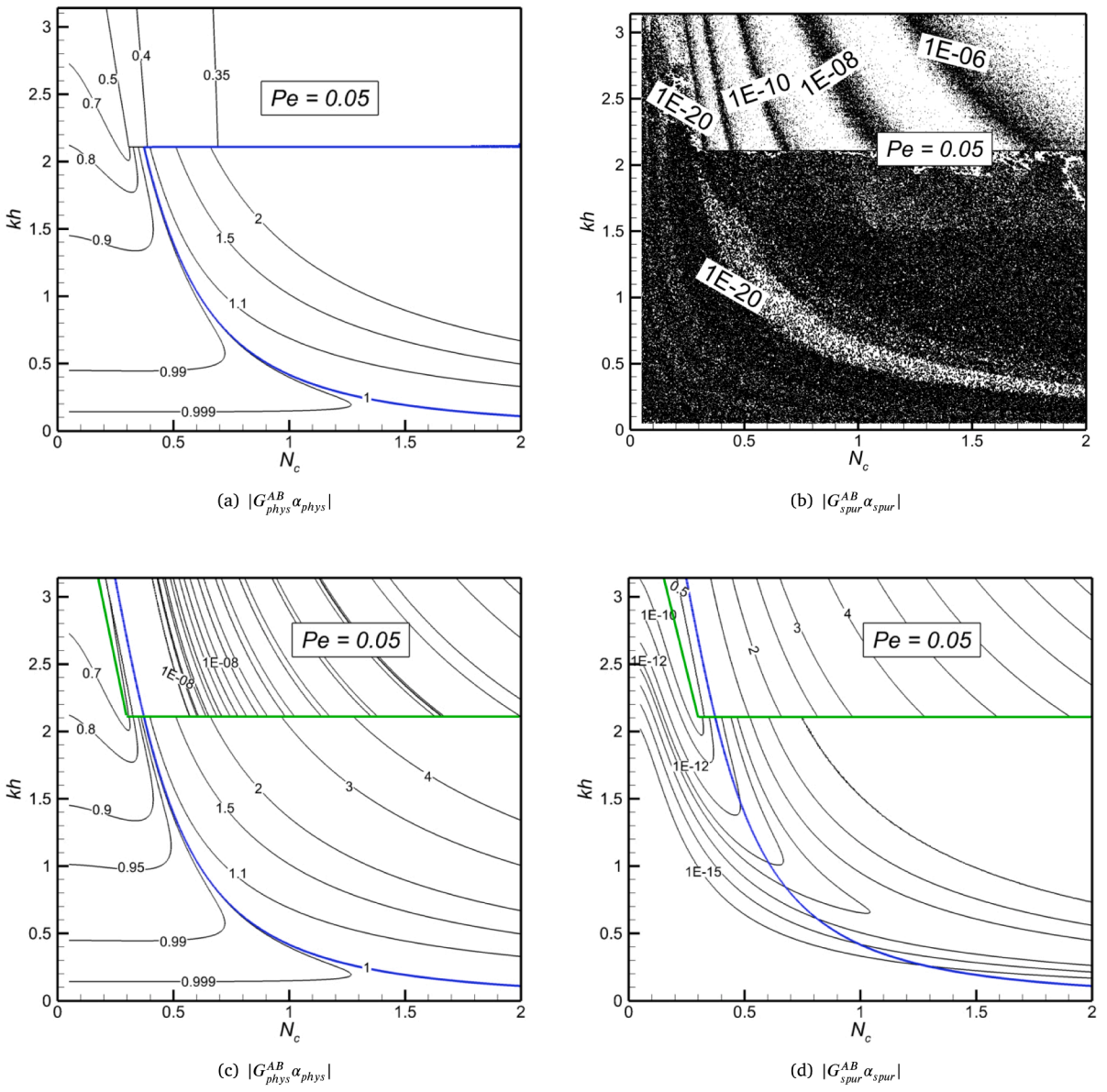


(a) $|G^{AB}_{phys}\alpha_{phys}|$ (b) $|G^{AB}_{spur}\alpha_{spur}|$

(c) $|G^{AB}_{phys}\alpha_{phys}|$ (d) $|G^{AB}_{spur}\alpha_{spur}|$

**Fig. 13.** Isolines of the physical and spurious modes obtained with an initial value of $\alpha_{spur} = 0$ (a, b) and $\alpha_{spur} = 10^{-8}$ (c, d) for $Pe = 0.05$. Green line - the discontinuity line, blue line - the stability border at ACS. (For interpretation of the references to colour in this figure legend, the reader is referred to the web version of this article.)

Fig. 14 shows the evolution of the solution RMS ($u_{RMS} = \sqrt{1/N \sum_{i=1}^{N} u(x_i)^2}$) normalized by its initial value for both $N_c$ values. As expected, for $N_c = 0.245$ the solution is stable for both initialization methods applied in the first step. Moreover, the initialization method has no visible impact on the solution at later times. The dashed and solid red curves are indistinguishable by eye. For $N_c = 0.25$, when the RK4 method is used for initialization, scenario no. 1 described above is observed: stability is lost after a short simulation time when $N_{c,stab} = 0.3575 \rightarrow 0.2475$. In contrast, when the AB method is employed for initialization, the solution remains stable for a very long time, consistent with scenario no. 2a. However, during this period, an initially zero contribution of the spurious mode grows due to round-off errors, as shown in Fig. 13b. Once it reaches a sufficiently high level, the solution error blows up (scenario no. 2b), and $u_{RMS}$ eventually rapidly grows, just as in the case of RK4 initialization.

The above illustration confirms that the spurious mode contribution to the total amplification factor of the AB method will always exist for some $Pe - N_c$ pairs, either due to numerical errors introduced by the two-time-level initialization procedure or due to unavoidable round-off errors. Although the origins of these errors differ, it has been shown that their long-term effects on stability characteristics are the same. In summary, the method used for the first step affects only the initial stage of the simulation. Moreover,

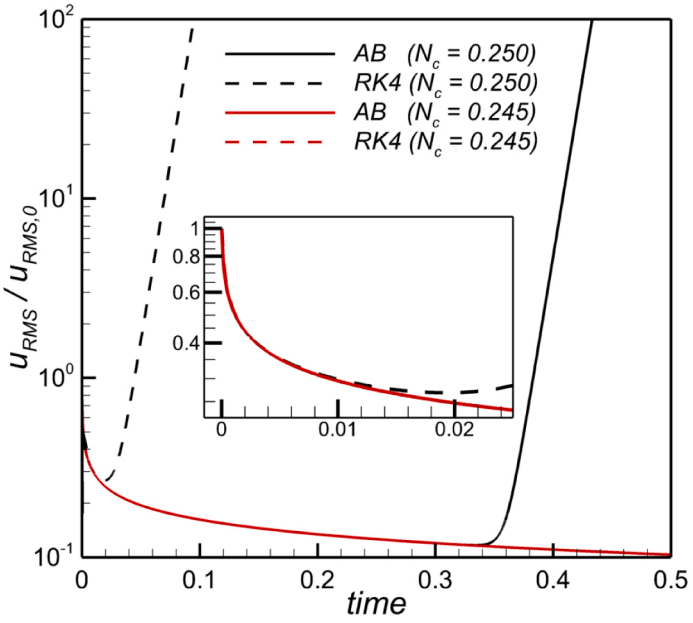


**Fig. 14.** Normalized solution root mean square for stable ($N_c = 0.245$) and unstable ($N_c = 0.25$) solutions initialized with AB and RK4 methods.

it does not imply that an initialization closer to the analytical solution, such as the 4th-order RK method used here, extends the simulation time over which the solution remains stable.

### 3.4. Adams-Moulton stability

GSA of the Adams-Bashforth method has quantified properties of physical and spurious modes that appear in the numerical solution. To complement this explicit time-stepping method, we follow an analogous framework for the implicit three-level Adams-Moulton method. As the implicit method is stable for higher Péclet numbers at which effects of the spurious mode are more outspoken, the analysis is performed at $Pe = 0.2$. Fig. 15 shows the total, physical, and spurious modes' amplification factors for the second time step using the RK4 initialization. In this case, an unusual region of instability is observed for $N_c \approx 0.3$ and $kh \approx 2.9$ where $|G_{tot}^{AM}| > 1$. This region appears to be linked to the initialization, as it disappears after additional time steps. This is shown in Fig. 16, presenting the amplification factor at ASC, obtained after several time steps. The instability line is also shifted significantly to lower CFL numbers compared to the results obtained in the second time step. Again, assuming $N_{c,stab}$ based on the stability map at $n = 2$ would lead to instability for long-term simulations, while adhering to the proper asymptotic stability result yields accurate and robust solutions. Similarly to the AB method, in ACS, physical and spurious modes are separated. In contrast to the AB method, we observe a large region where the method remains stable ($N_c \leq 0.95$), albeit with only the spurious mode active. One should note that a decrease in $N_c$ cannot eliminate the spurious mode, but it can limit the range of small scales affected by the spurious mode. This would be the case for $N_c$ for which the green discontinuity line is curved and oriented towards the border $kh = \pi$.

## 4. Stability regions for Adams-Bashforth and Adams-Moulton integration methods

In this section, we identify general stability regions in the $Pe - N_c$ plane in ACS. We explicitly derive the limiting $Pe$ number for which the occurrence of the spurious mode can be avoided by reducing $N_c$. So far, three different sets of test cases have been analyzed, concentrating on the AB and AM methods. In the first set of cases, we considered the AB method at small $Pe = 0.01$. It has been shown that the spurious mode is negligible and the solution is dominated by the physical mode for all scales $kh < \pi$ and all CFL numbers $N_c < N_{c,stab}$ (see Fig. 4). For higher $Pe = 0.05$, a part of the stability region was dominated by the spurious mode, affecting the smaller scales. In this case, the spurious mode can be eliminated by choosing a sufficiently small $N_c$, as can be seen in Fig. 6. The stability map for the implicit AM method was considered for $Pe = 0.2$. In this case, the spurious mode dominates the smaller scales for all $N_c$ numbers, including the limit $N_c \to 0$, i.e., even in the limit toward a zero time step, as illustrated in Fig. 16.

To understand the differences between these test cases, we can compare the physical modes of the AB method for $Pe = 0.01$ presented in Fig. 4 and for $Pe = 0.05$ shown in Fig. 5. For the smaller Péclet number, the physical mode is smooth in the whole $kh - N_c$ plane. At the same time, for $Pe = 0.05$, there is a discontinuity in the distribution of the physical/spurious modes where they abruptly grow/drop. As discussed in Section 2.2, this discontinuity is caused by the change of sign of the imaginary part of the discriminant in (30). It is defined as

$$Im(\Delta) = N_c(kh)\left(\frac{9}{2}Pe(kh)^2 - 1\right) \tag{59}$$

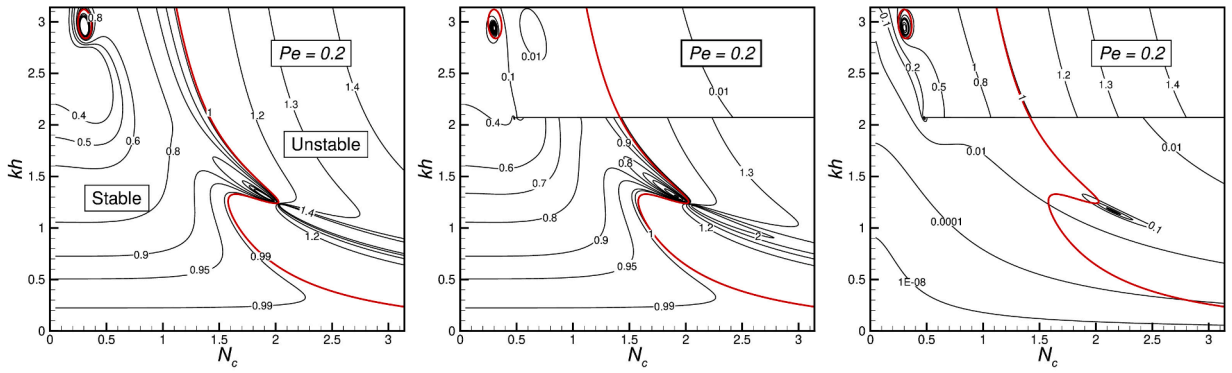


**Fig. 15.** Isolines of the total amplification factor (a) and the physical (b) and spurious (c) modes' factor for $Pe = 0.2$. Results at the time-step $n = 2$ applying the AM method with the RK4 method for the initialization.

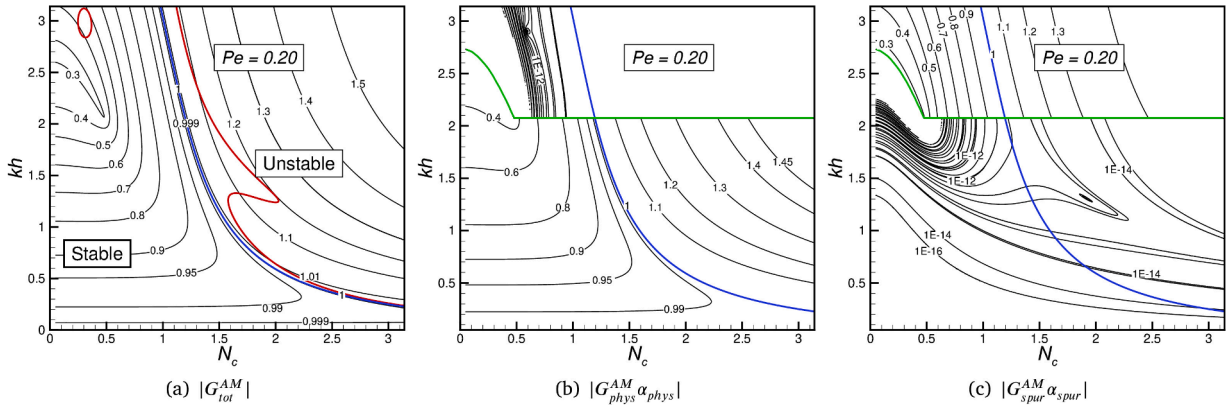


**Fig. 16.** Isolines of the total amplification factor (a) and the physical (b) and spurious (c) modes' factors for $Pe = 0.2$. Results at ACS were obtained by applying the AM with the RK4 method for the initialization. Green line - the discontinuity line, red line - the stability border at $n = 2$, blue line - the stability border at ACS. (For interpretation of the references to colour in this figure legend, the reader is referred to the web version of this article.)

Hence, the critical Péclet number below which the spurious mode does not appear in ACS can be found from the following condition:

$$\mathrm{Im}(\Delta(kh = \pi)) < 0 \tag{60}$$

ensuring that the imaginary part of the discriminant is always negative in the whole $kh$ range, which leads to the definition of a first critical Péclet number as $Pe^I_{cr} = 2/(9\pi^2) \approx 0.022$. For the AM method, the imaginary part of the discriminant (45) is given as

$$\mathrm{Im}(\Delta) = N_c(kh)\left(\frac{7}{6}Pe(kh)^2 - 1\right) \tag{61}$$

and, similarly, it leads to the critical Péclet number $Pe^I_{cr} = 6/(7\pi^2) \approx 0.087$. Fig. 17 shows stability diagrams in the $Pe - N_c$ plane divided into three subregions for which the simulations are stable. The stability border (blue line) denotes the minimum $N_c$ values found on the line $|G_{tot}| = 1$. Worth noting is that both for AB and AM methods, there is a maximum Péclet number ($Pe_{stab}$) above which the solution is unstable for $N_c > 0$. An illustration of this situation is the case of applying the AB method for $Pe = 0.2$, see the stability map in Fig. 1. The stability limits in terms of the Péclet number for $N_c \to 0$ are equal to $Pe_{stab} = 1/\pi^2$ (AB) and $Pe_{stab} = 6/\pi^2$ (AM).

The critical Péclet numbers $Pe^I_{cr}$ are marked by vertical black lines in Fig. 17. For $Pe > Pe^I_{cr}$, the spurious mode may appear for $kh > \sqrt{2/9Pe}$ and $kh > \sqrt{6/7Pe}$, for the AB and AM methods, respectively. However, its occurrence is conditioned by $N_c$ and can be avoided provided that $N_c$ is sufficiently small. These $N_c$ values are indicated by the green lines. Referring to the AB method and the stability map for $Pe = 0.05$ presented in Fig. 6, this line shows $N_c = N_{c,spur}$ at $kh = \pi$. For $N_{c,spur} < N_c < N_{c,stab}$ the solution is stable, but some range of scales evolves in time with the spurious mode (grey region in Fig. 17). The values of $N_{c,spur}$ are determined by iteratively searching for $N_c$ for which $\alpha_{phys,spur}$ at $kh = \pi$ jumps to one or zero. It can be seen that increasing the Péclet number causes $N_{c,spur}$ shifts towards smaller $N_c$ up to $N_c = 0$. This defines the second critical Péclet number $Pe^{II}_{cr}$, which with the assumption $kh = \pi$ and $N_c = 0$ can be obtained analytically from the condition $|G_{phys}| = |G_{spur}|$. They are equal to $Pe^{II}_{cr} = 2/(3\pi^2)$, $Pe^{II}_{cr} = 3/(2\pi^2)$ for the AB and AM methods. In the range $Pe^{II}_{cr} < Pe < Pe_{stab}$, the spurious mode is always present in the solution. An example of this

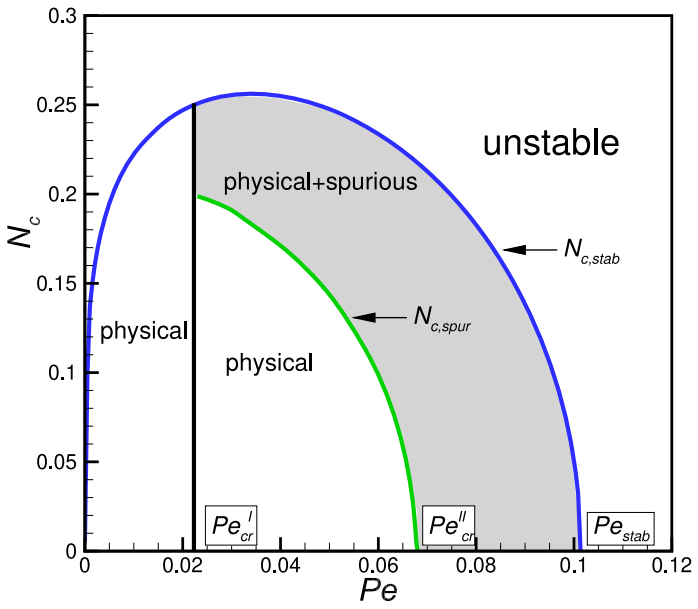


(a)

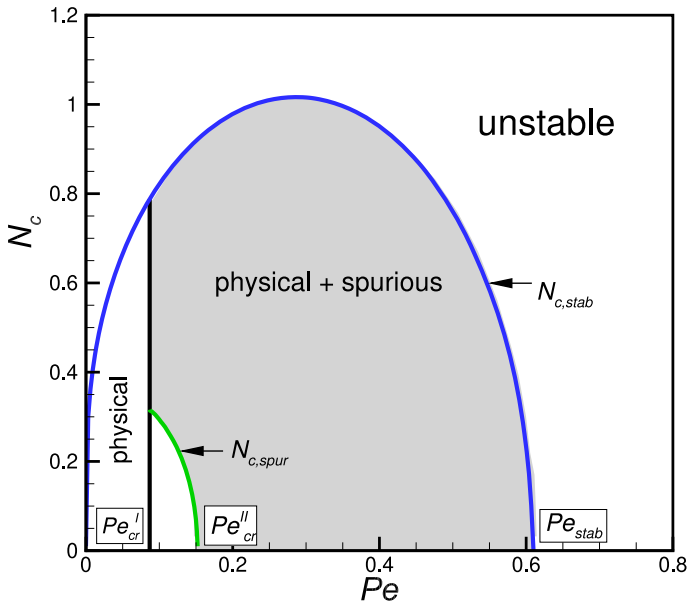


(b)

**Fig. 17.** Stability maps on the $Pe - N_c$ planes for the Adams-Bashforth (a) and Adams-Moulton (b) methods. The critical and stable $Pe$ numbers correspond to the values where the black, green, or blue line crosses the $Pe$-axis. (For interpretation of the references to colour in this figure legend, the reader is referred to the web version of this article.)

situation is applying the AM method for $Pe = 0.2$. As can be seen in Fig. 16, in this case, lowering $N_c$ leads only to a narrower range of small scales contaminated by the spurious mode.

## 5. Accuracy vs. stability

The analysis presented so far has focused almost exclusively on stability, with particular attention paid to the regions of the stability maps influenced by the physical and spurious modes. The issue of solution accuracy has not yet been addressed explicitly,

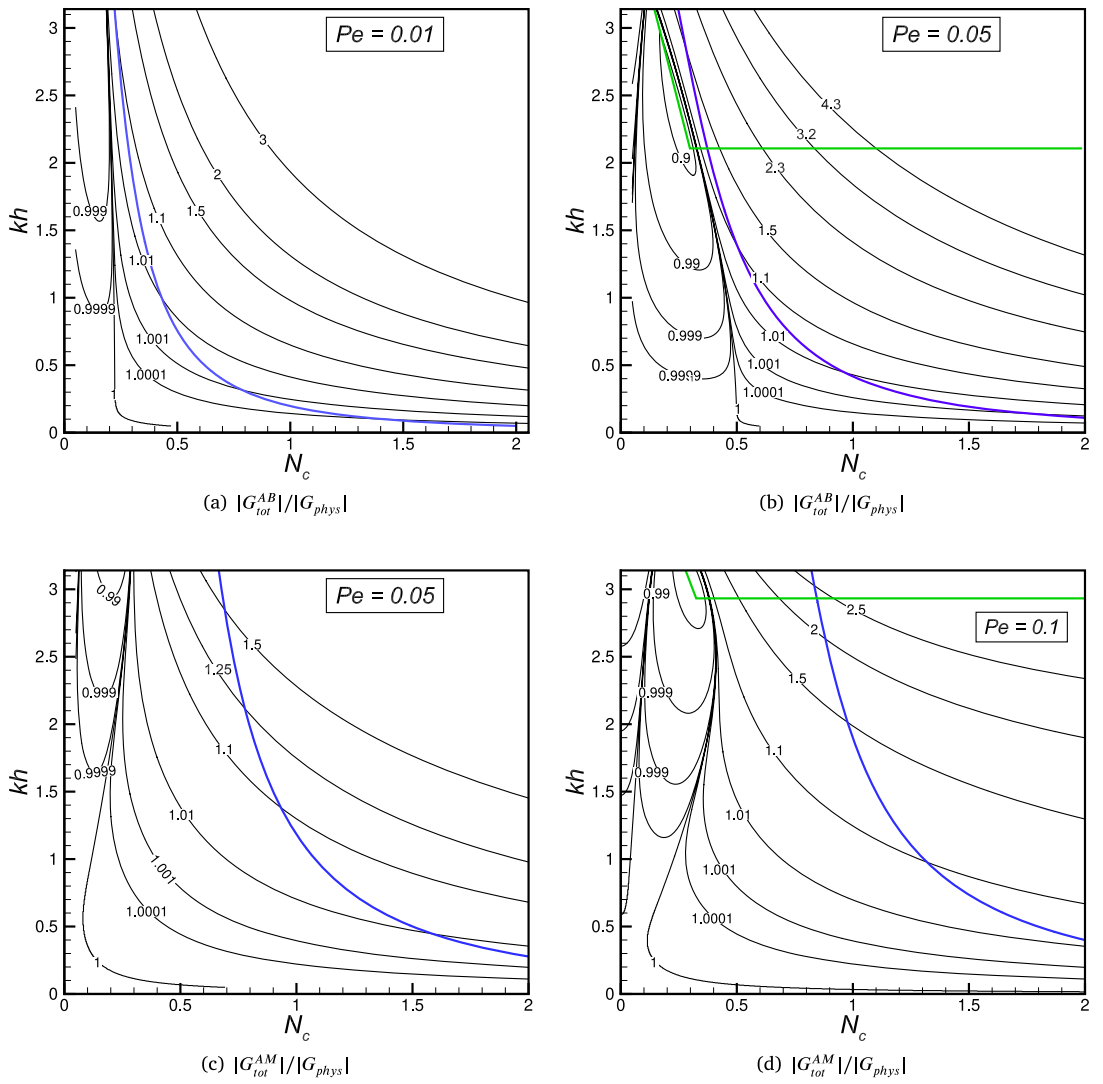


(a) $|G_{tot}^{AB}|/|G_{phys}|$ (b) $|G_{tot}^{AB}|/|G_{phys}|$

(c) $|G_{tot}^{AM}|/|G_{phys}|$ (d) $|G_{tot}^{AM}|/|G_{phys}|$

**Fig. 18.** Contour maps of the ratios of the numerical total amplification factor to the physical amplification factor for the AB method ($|G_{tot}^{AB}|/|G_{phys}|$) at $Pe = 0.01$ (a) and $Pe = 0.05$ (b) and for the AM method ($|G_{tot}^{AM}|/|G_{phys}|$) at $Pe = 0.05$ (c) and $Pe = 0.1$ (d). The stability boundary is indicated in blue, while the occurrence of spurious modes is the region above the green line. (For interpretation of the references to colour in this figure legend, the reader is referred to the web version of this article.)

although some insight can be gained from Figs. 11-12, which show the physical and spurious components of the numerical viscosity, phase speed, and group velocity.

In this section, we analyze the distributions of the total numerical amplification factors ($|G_{tot}|$) with respect to the growth rate obtained from the exact solution ($|G_{phys}|$) of the AB and AM methods at specific Péclet number regimes. The ratio $|G_{tot}|/|G_{phys}|$ is an easy and insightful measure of solution accuracy. Fig. 18 shows $|G_{tot}^{AB}|/|G_{phys}|$ for the AB method at $Pe = 0.01$ and $Pe = 0.05$ and $|G_{tot}^{AM}|/|G_{phys}|$ for the AM method at $Pe = 0.05$ and $Pe = 0.1$. Note that the ratio $|G_{tot}^{AB,AM}|/|G_{phys}| > 1$ denotes damping smaller than that stemming from the physical mechanism ($\nu_{num}/\nu < 1$, see Eq. (14)). According to the stability diagrams in Fig. 17, the AB method at $Pe = 0.01$ and the AM method at $Pe = 0.05$ are free from the influence of spurious modes ($Pe < Pe_{cr}^{I}$). In contrast, the Péclet numbers $Pe = 0.05$ for the AB method and $Pe = 0.1$ for the AM method lie within the range $Pe_{cr}^{I} < Pe < Pe_{cr}^{II}$, in which $N_c$ determines whether the corresponding $kh$ scales evolve according to the physical or the spurious mode. In general, the solution accuracy significantly drops when $N_c \to N_{c,stab}$. The decrease in accuracy is stronger for the AM method, which allows the use of larger $N_c$, while remaining stable, and for which the temporal discretization error scales as $N_c^3$ ($\propto N_c^2$ for AB). Regarding the characteristics of the ratio $|G_{tot}^{AB,AM}|/|G_{phys}|$, we observe that when approaching the stability limit $|G_{tot}^{AB,AM}|/|G_{phys}| > 1$. On the other hand, when $N_c \to 0$, the solution becomes more and more accurate. Focussing on Fig. 18b,d showing $|G_{tot}^{AB,AM}|/|G_{phys}|$ in the regimes $Pe_{cr}^{I} < Pe < Pe_{cr}^{II}$ we see that in the region in which the spurious mode is dominant ($kh$ above the green line), corresponding small structures would be calculated the least accurately. However, it cannot be said that for a particular $N_c < N_{c,stab}$ the solution to these

scales would be fundamentally worse compared to those in the region in which the physical mode is dominant ($kh$ below the green line).

Based on the presented examples, we infer that for a given Péclet number, keeping $N_c < N_{c,spur}$ leads to $|G_{tot}^{AB,AM}|/|G_{phys}| \approx 1$ along the entire $kh$ range. However, applying a small $N_c$ directly corresponds to a larger number of time steps needed to advance the solution over a given time interval. It may turn out that the computational efficiency of multi-time-level methods compared to a two-time-level method of the same order, as discussed in the introduction, does not bring benefits when the accuracy across all solution scales is the priority. Furthermore, it should be noted that the condition $N_c < N_{c,spur}$ cannot be fulfilled when $Pe > Pe_{cr}^{II}$. In such cases, two-time-level methods can be generally preferred. The issues of solution accuracy and efficiency in connection with the presently established stability diagrams for the entire range $Pe < Pe_{stab}$, are subject of ongoing research in which we also include a comparison with two-time-level methods.

## 6. Conclusions

A global spectral analysis has been performed for the Fourier-discretized convection–diffusion equation combined with a three-level time-integration method. The explicit Adams–Bashforth and implicit Adams–Moulton methods were analyzed, both of which are known to admit two solution modes: the physical and the spurious mode. The overall stability of the simulation is determined by the superposition of these modes. During integration, the solution approaches the asymptotic converged state, and the long-term stability of the methods is governed by the amplification factors established in this state. Once the solution reaches the converged state, the fraction of either the spurious or the physical mode becomes 0 or 1, meaning that the two modes do not coexist.

The spurious mode is primarily present for small scales ($kh \to \pi$) within the stability region and determines the stability boundary. Its occurrence was initially expected to be triggered solely by the difference between the amplification factor of the method used in the first time step and the physical mode of the three-level method. This reasoning suggested that stability might be improved by eliminating the spurious mode from the initial condition through a suitable choice of the initialization method. However, numerical tests have demonstrated that this idea cannot be realized in practical computations due to truncation and round-off errors. In practice, the choice of the method used in the first step of the time integration does not alter the overall stability characteristics in the asymptotically converged state.

Finally, the stability characteristics of the three-level methods considered in this paper were summarized in the form of a stability diagrams in the Péclet–CFL space. These diagrams show that the region in which the spurious mode is present grows with the Péclet number. In particular, it identifies critical CFL and Péclet numbers such that

- for $Pe < Pe_{cr}^{I}$ the solution is governed solely by the physical mode for any $N_c$ within the stability limit $N_c < N_{c,stab}$;
- for $Pe_{cr}^{I} < Pe < Pe_{cr}^{II}$ the solution is governed either by the physical or the spurious mode, depending on $kh$, but the appearance of the latter can be avoided by selecting a sufficiently small CFL number, $N_c < N_{c,spur}$;
- for $Pe > Pe_{cr}^{II}$ the spurious mode appears for the entire range of $N_c$, even in the limit of a vanishing time step.

In future studies, an analysis of three-level time-integration methods will be conducted across different spatial discretizations, including explicit and implicit finite-difference schemes of various orders. Moreover, considering the inherent constraints of three-level methods — such as the need to preserve only the physical mode and suppress spurious solutions — a comparative investigation with two-level methods will be conducted, focusing on accuracy and efficiency. Two-level methods, known for being free of spurious modes across the entire stability region, are the methods of choice for many simulation studies and thus serve as an important benchmark for evaluating the effectiveness and practicality of multi-level approaches. Such a comparison will provide valuable insights into the trade-offs between computational efficiency, stability, and physical fidelity, guiding the selection of optimal time-integration strategies for a wide range of numerical simulations.

The analysis focused on the linear convection–diffusion equation. This provides the two main fundamental transport mechanisms in fluid mechanics, illustrating all the dynamic richness that Adams-Bashforth and Adams-Moulton time integration represent. Since all analysis steps can be related exactly and analytically to algebraic operations, we could show that the characteristic equation of these three-level schemes reduces to a quadratic polynomial, for which the full mode analysis can be carried out in closed form. The emergence of spurious modes and their relation to physical dynamics were displayed in terms of the $Pe - N_c$ stability domain, yielding a new result in the literature of direct use to researchers in the field. Our study represents a first step toward analyzing more realistic problems and a wider range of time integration methods, including two-time-level Runge-Kutta methods. This is the subject of ongoing research, which will provide a direct comparison regarding convergence, computational costs, and accuracy of the AB and AM methods in the regimes at which our current analysis has shown that spurious modes are not present. In addition to the numerical aspects arising from comparing the AB and AM methods with spurious-mode-free Runge-Kutta schemes, the fluid-mechanical consequences will be clarified for incompressible Navier-Stokes dynamics using simulations of homogeneous isotropic turbulence. That way, the role of spurious modes in numerical modelling of small-scale turbulence will be clarified. This will be the topic of an applied study, complementing the selected numerical emphasis chosen in this paper.

## CRediT authorship contribution statement

**A. Boguslawski:** Writing – review & editing, Writing – original draft, Visualization, Validation, Supervision, Software, Resources, Project administration, Methodology, Investigation, Funding acquisition, Formal analysis, Conceptualization; **A. Tyliszczak:** Writing

– review & editing, Writing – original draft, Methodology, Investigation, Formal analysis, Conceptualization; **B. J. Geurts:** Writing – review & editing, Writing – original draft, Methodology, Investigation, Formal analysis, Conceptualization.

## Declaration of competing interest

The authors declare that they have no known competing financial interests or personal relationships that could have appeared to influence the work reported in this paper.

## Acknowledgements

This research was funded by the National Science Center, Poland, under Project No. 2023/49/B/ST8/00773, and was supported by statutory research funds from the Silesian University of Technology and the Częstochowa University of Technology (BS/PB 1-100-301/2026/P). The second author acknowledges support from the Polish National Agency for Academic Exchange under the PHC Polonium Program. High-performance computing resources were provided by the PLGrid infrastructure under Computational Grant No. PLG/2025/018453.

## Data availability

No data was used for the research described in the article.

## References

[1] P. Sagaut, V.K. Suman, P. Sundaram, M.K. Rajpoot, Y.G. Bhumkar, S. Sengupta, A. Sengupta, T.K. Sengupta, Global spectral analysis: review of numerical methods, Comput. Fluids 261 (2023) 105915–87.
[2] T.K. Sengupta, G. Generiwal, S. De, Analysis of central and upwind compact schemes, J. Comput. Phys. 192 (2) (2003) 677–694.
[3] T.K. Sengupta, V. Lakshmanan, V.V. S.N. Vijay, A new combined stable and dispersion relation preserving compact scheme for non-periodic problems, J. Comput. Phys. 228 (2009) 3048–3071.
[4] T.K. Sengupta, High accuracy computing methods: fluid flows and wave phenomena, Cambridge University Press, 2013.
[5] T.K. Sengupta, V.K. Suman, P. Sundaram, A. Sengupta, Analysis of pseudo-spectral methods used for numerical simulation of turbulence, 2021, arXiv:2109.00255.
[6] V.K. Suman, P. Sundaram, A. Sarkar, T.K. Sengupta, Direct simulation of two-dimensional flows by pseudo-spectral method: special features and validations by taylor–green vortex problem, Comput. Fluids 300 (2025) 106754.
[7] T.K. Sengupta, A. Dipankar, A comparative study of time advancement methods for solving navier–stokes equations, J. Sci. Comput. 21 (2) (2004) 225–250.
[8] T.K. Sengupta, S.K. Sircar, A. Dipankar, High accuracy schemes for DNS and acoustics, J. Sci. Comput. 26 (2) (2005) 151–193.
[9] S.B. Pope, Turbulent Flows, Cambridge University Press, 2000.
[10] P. Sagaut, Large eddy simulation for incompressible flows, Springer, 2001.
[11] G.J. Haltiner, R.T. Williams, Numerical Prediction and Dynamic Meteorology, John Wiley & Sons, New York, 2nd edition, 1980.
[12] D.K. Lilly, On the computational stability of numerical solution of time-dependent nonlinear geophysical fluid dynamics problems, Mon. Weather Rev. 93 (1) (1965) 11–26.
[13] D.R. Durran, Numerical Methods for Wave Equations in Geophysical Fluid Dynamics, Springer, New York, 1999.
[14] J. Kim, P. Moin, R.D. Moser, Turbulence statistics in fully developed channel flow at low Reynolds number, J. Fluid Mech. 177 (1987) 133–166. Uses a second-order Adams–Bashforth scheme for time advancement.
[15] H. Abe, H. Kawamura, Y. Matsuo, Direct numerical simulation of a fully developed turbulent channel flow with respect to reynolds number dependence, J. Fluids Eng. 123 (2001) 382–393. Convection terms advanced using a second-order Adams–Bashforth scheme.
[16] V.K. Suman, T.K. Sengupta, C.J.D. Prasad, K.S. Mohan, D. Sanwalia, Spectral analysis of finite difference schemes for convection diffusion equation, Comput. Fluids 150 (2017) 95–114.
[17] T.K. Sengupta, A. Sengupta, K. Saurabh, Global spectral analysis of multi-level time integration schemes: numerical properties for error analysis, Appl. Math. Comput. 304 (2017) 41–57.
[18] G. Dahlquist, A special stability problem for linear multistep methods, BIT Numer. Math. 3 (1) (1963) 27–43.
[19] A. Quarteroni, R. Sacco, F. Saleri, Numerical Mathematics, Springer, 2007.
[20] C. Canuto, M.Y. Hussaini, A. Quarteroni, T.A. Zang, Spectral methods in fluid dynamics, Springer-Verlag, 1988.
[21] B.J. Geurts, Elements of Direct and Large-Eddy Simulation, Edwards Publishing, 2003.
[22] R. Vichnevetsky, J.B. Bowles, Fourier analysis of numerical approximations of hyperbolic equations, SIAM, Philadelphia, 1982.
[23] S.K. Lele, Compact finite difference with spectral-like resolution, J. Comput. Phys. 103 (1992) 16–42.
[24] L. Caban, A. Tyliszczak, High-order compact difference schemes on wide computational stencils with a spectral-like accuracy, Comput. Math. Appl. 108 (2022) 123–140.